Displacement of extracellular chloride by sulfated glycosaminoglycans of the brain's extracellular matrix*

Kieran P Normoyle,[1,2] Kyle P Lillis,[1,2] Kiyoshi Egawa,[3] Melanie A McNally,[1,2] Mousumi Paulchakrabarti,[4] Biswa P Coudhury,[4] Lauren Lau,[1,2] Fu Hung Shiu,[1,2] and Kevin J Staley[1,2]

1. Department of Neurology, Division of Child Neurology, Massachusetts General Hospital, Boston, MA, United States
2. Department of Neurology, Harvard Medical School, Boston, MA, United States
3. Department of Medicine, Hokaiddo University, Sapporo, Hokaiddo, Japan
4. GlycoAnalytics Core, University of California San Diego, La Jolla, CA, United States

First author profile: Kieran Normoyle completed MS degrees in Chemistry and Physiology before completing his MD and PhD in Molecular and Integrative Physiology under the supervision of William M Brieher in 2015. His work focuses on understanding the process of epileptogenesis, particularly the role of chloride transport and its effects on both GABAergic signaling and neuronal volume regulation. His goal is to understand how neurons utilize intra- and extracellular structural features regulated on differing time scales to properly function both individually and as part of a larger information storage and retrieval system, and how failure to do so leads to seizure and epilepsy.

Key Points Summary

- Extracellular chloride concentrations in the brain were measured using a new chloride-sensitive organic fluorophore and two photon fluorescence lifetime imaging.
- *In vivo*, the extracellular chloride concentration was spatially heterogenous and only half of the CSF chloride concentration
- Stable displacement of extracellular chloride by immobile extracellular anions was responsible for the low extracellular chloride concentration
- The changes in extracellular chloride were of sufficient magnitude to alter the conductance and reversal potential of $GABA_A$ chloride currents
- The stability of the extracellular matrix, the impact of the component immobile anions including sulfated glycosaminoglycans on extracellular chloride concentrations, and the consequent effect on $GABA_A$ signaling suggests a previously unappreciated mechanism for modulating $GABA_A$ signaling.

* This manuscript was first published as a preprint: Normoyle KP, Lillis KP, Egawa K, McNally MA, Paulchakrabarti M, Coudhury BP, and Staley KJ (2022). Displacement of extracellular chloride by sulfated glycosaminoglycans of the brain's extracellular matrix. bioRxiv. https://doi.org/10.1101/2022.12.28.522113

Abstract

GABA is the primary inhibitory neurotransmitter. Membrane currents evoked by $GABA_A$ receptor activation have uniquely small driving forces: their reversal potential (E_{GABA}) is very close to the resting membrane potential. As a consequence, $GABA_A$ currents can flow in either direction, depending on both the membrane potential and the local intra and extracellular concentrations of the primary permeant ion, chloride (Cl). Local cytoplasmic Cl concentrations vary widely due to displacement of mobile Cl ions by relatively immobile anions. Here we use new reporters of extracellular chloride (Cl^-_o) to demonstrate that Cl is displaced in the extracellular space by high and spatially heterogenous concentrations of immobile anions including sulfated glycosaminoglycans (sGAGs). Cl^-_o varies widely, and the mean Cl^-_o is only half the canonical concentration, i.e. the Cl concentration in the cerebrospinal fluid. These unexpectedly low and heterogenous Cl^-_o domains provide a mechanism to link the varied but highly stable distribution of sGAGs and other immobile anions in the brain's extracellular space to neuronal signal processing via the effects on the amplitude and direction of $GABA_A$ transmembrane Cl currents.

Introduction

$GABA_A$ synapses comprise the primary output for inhibitory interneurons in the brain (Hu *et al.*, 2014; Tremblay *et al.*, 2016). A unique feature of $GABA_A$ synapses are the very small driving forces for ion flux through open $GABA_A$ receptor-operated membrane channels. The reversal potential for the primary permeant ion, chloride, is usually within a few mV of the neuronal resting membrane potential (RMP) (Thompson *et al.*, 1988) and may even be positive to RMP (Staley & Mody, 1992; Tyzio *et al.*, 2008). This low driving force makes possible a novel form of synaptic plasticity at $GABA_A$ synapses: the direction of current flow, i.e. the effect of $GABA_A$ receptor activation on the resting membrane potential, can be reversed by low millimolar alterations in the local chloride concentration (Coombs *et al.*, 1955). Such physiological variance is routinely observed in individual studies (Ebihara *et al.*, 1995; Huberfeld *et al.*, 2007) and is likely to underlie the 25 mV range of reported group mean reversal potentials in 20 recent studies of evoked $GABA_A$ currents recorded with gramicidin perforated patch electrodes in area CA1 of the hippocampus (tabulated in (Rahmati *et al.*, 2021). This variance has substantial effects on synaptic signaling: the reversal potential of $GABA_A$ currents evoked in a single pyramidal cell by stimulation of 8 different presynaptic interneurons also varied by over 20 mV (Rahmati *et al.*, 2021).

We have proposed that the intracellular chloride concentration (Cl^-_i) is not monotonic across the neuronal cytoplasm, but rather varies inversely with the local concentration of macromolecular anions that comprise the vast majority of intracellular anions (Glykys *et al.*, 2014a; Rahmati *et al.*, 2021). This phenomenon is known as Donnan exclusion (Marinsky, 1985; Helfferich, 1995; Fatin-Rouge *et al.*, 2003; Epsztein *et al.*, 2018; Gao *et al.*, 2022). Mobile ions, in this case Cl, are repelled by relatively immobile ions such as proteins with negative surface charges. Many proteins such as gephyrin that are associated with $GABA_A$ synapses bear large negative surface charges (Sola *et al.*, 2001), suggesting that variance in the $GABA_A$ reversal potential (E_{GABA}) is determined by local fixed cytoplasmic charge densities. However, E_{GABA} is not determined solely by Cl^-_i but rather by the ratio of intra- to extracellular permeant ions. This

raises the possibility that spatial variance in the extracellular Cl concentration (Cl^-_o) could also be an important determinant of E_{GABA}.

The displacement of Cl^- by fixed negative charges should also occur in the extracellular space, where the high negative charge density of several classes of functionalized macromolecules are anchored to the cell membrane either directly or indirectly. Gangliosides typically bearing one to three – or more, though rarely – carboxylate groups in the form of sialic acid groups are present in the extracellular space of human cerebral cortex (Schnaar *et al.*, 2014) and are concentrated within the synaptosomal fraction (Svennerholm, 1980). Together with the polysulfated glycosaminoglycans (GAGs) that are a major constituent of the extracellular matrix (Karamanos *et al.*, 2021), which have been reported to be as high as the Cl^- concentration in the CSF (Urban *et al.*, 1979; Chahine *et al.*, 2005; Morawski *et al.*, 2015), we calculate that total extracellular fixed anions are in excess of 50mM (see Methods; Schnaar *et al.*, 2014). Thus some to all of the local Cl^-_o could be displaced, depending on local anionic density and the degree of GAG sulfation. Such displacement has been most clearly demonstrated in the chondroitin sulfate-rich matrix of cartilaginous tissue, where the negative charge density of the extracellular matrix can reach 400 meq / liter (Lesperance *et al.*, 1992), but dozens of mM of Cl^-_o are also displaced by sulfated GAGs in tissues such as skin (Titze *et al.*, 2004). Mucous, which comprises the extracellular space for airway epithelial cells, is also rich in polysulfated GAGs that displace about half of the Cl^-_o (Reuter *et al.*, 1998). Given this evidence for sulfated GAGs displacing Cl^-_o and the commercial availability of exogenous matrix metalloprotease (MMP) analog chondroitinase, we chose to focus on the role of extracellular sulfated GAGs and, in particular, the role of chondroitin sulfate.

Many findings suggest that the brain Cl^-_o is lower than the canonical value. Xray emission spectroscopy of the extracellular space has demonstrated sulfate concentrations as high as 100 mM (Morawski *et al.*, 2015). Astrocytic buffering of Cl^-_o (Egawa *et al.*, 2013) would not be necessary if Cl^-_o were indeed > 100 mM. The gating of Group II and III metabotropic glutamate receptors, kainate receptors, acid-sensing membrane ion channels, and the transport rate of the GlyT1 glycine transporter are all strongly modulated by Cl^-_o over the entire range of 1 - 100 mM (Kuang & Hampson, 2006; Plested & Mayer, 2007; Kusama *et al.*, 2010; DiRaddo *et al.*, 2015; Tora *et al.*, 2018; Zhang *et al.*, 2021). Such strong modulation by low Cl^-_o would not make sense if Cl^-_o was uniformly > 100 mM.

Studies of Cl^-_o are few, particularly in live mammalian tissue, and have been carried out with ion-sensitive electrodes that sample only one microenvironment (Nicholson & Kraig, 1975). Our prior work suggested that the local chloride concentration varies widely as a function of the local concentration of immobile anions (Rahmati *et al.*, 2021). Earlier results from our group (Glykys *et al.*, 2014a) have suggested that physiological Cl^-_o is lower than that measured with ion-sensitive electrodes, and we hypothesized that the large sample sizes provided by fluorometric imaging techniques might provide the most robust measure of the extracellular chloride distribution.

Although a fluorometric study of Cl^-_o would provide a noninvasive means to establish the distribution of chloride in the extracellular space, no suitable Cl-sensitive organic fluorophores exist, and transgenic fluorophores such as SuperClomeleon (Grimley *et al.*, 2013) and CloPhensor (Sato *et al.*, 2017) are not distributed in the extracellular space. We therefore developed a chloride-sensitive fluorophore (Normoyle *et al.*, 2024) from previously described organic backbones (Biwersi *et al.*, 1992; Biwersi *et al.*, 1994) that satisfied the following criteria.

121 First, the fluorophore should be sensitive to Cl in the range of the extracellular chloride
122 concentration i.e., up to 100 mM; available fluorophores have been optimized for the low
123 millimolar chloride concentrations of the cytoplasm. Second, the fluorophore should report Cl
124 independently of the concentration of fluorophore. Ratiometric fluorophores suitable for the
125 extracellular space do not exist, so we used **F**luorescence **L**ifetime **Im**aging (FLIM) (Kaneko *et*
126 *al.*, 2004) to remove the dependence of the fluorescence emission on fluorophore
127 concentration. Third, the fluorophore should be constrained to the extracellular space, for which
128 dextran conjugation is optimal (Xiao *et al.*, 2008; Tønnesen *et al.*, 2018). Fourth, the
129 fluorophore should be excited by wavelengths that are not damaging to brain tissue, i.e. below
130 the ultraviolet range and in the visible or infrared range. Fifth, many Cl sensors are also
131 sensitive to pH (Kuner & Augustine, 2000; Grimley *et al.*, 2013), so a pH-insensitive fluorophore
132 would be ideal. Finally, the fluorophore needs to be sufficiently bright so that its emission can be
133 reliably distinguished from autofluorescence.

134 Here, we utilize a newly synthesized Cl-sensitive fluorophore that meets these 6 criteria to
135 demonstrate: stable Donnan exclusion of chloride by immobile extracellular anions such as
136 sulfates fixed to GAG-like carbohydrate polymers; directly measured Cl^-_o of *in vitro* and *in vivo*
137 brain tissue that is much lower than cerebrospinal or plasma chloride; a remarkable spatial
138 variance in Cl^-_o; and, as evidence that Cl^-_o is determined by Donnan exclusion of Cl by sulfated
139 moieties such as GAGs, Cl^-_o increases after release of immobile sulfates by exogenous
140 chondroitinase.

141

142 **Methods**

143 Ethical Approval: All animals are housed in a facility with on-call veterinary team and have free
144 access to food water in accordance with MGH IACUC animal welfare board regulations,
145 conforming to Grundy 2015 principles and regulations (protocol 2018N000221). Isofluorane
146 anaesthesia was induced by inhalation through a nosecone at 5mL/min and maintained at 1-
147 2mL/min for the duration of the experiment, checking frequently for signs of adequate
148 anaesthesia. All surgeries performed were acute (non-survival) experiments after which mice
149 were administered maximum anaesthesia (5mL/min isofluorane) and euthanized by
150 decapitation.

151 General: Chemicals were purchased from Sigma-Aldrich (St Louis, MO) unless otherwise noted.
152 Solutions are brought up in distilled water unless otherwise noted. Standard aCSF was brought
153 up in 18MΩ water and consisted of (in mM): NaCl 126; KCl 3.5; $CaCl_2$ 2; $MgCl_2$ 1.3; NaH_2PO4
154 1.2; Glucose 11; $NaHCO_3$ 15. Low chloride aCSF variant was identical except that sodium
155 gluconate was substituted for NaCl, resulting in 10mM Cl^-. Calibration solutions were made by
156 mixing appropriate proportions of standard aCSF with low chloride aCSF such that a chloride
157 and gluconate sum total of 136mM was maintained while Cl^- ranged from 10 to 136mM.
158 Colorimetric assays were read using a Wallac Victor-2 1420 spectrophotometer with a halogen
159 continuous wave light source and spectral line filters at listed wavelength +/- 5 to 10nm.
160 Centrifugation steps were accomplished in a tabletop Eppendorf 5417R microcentrifuge. Reflux
161 apparatus for synthesis consisted of a recirculating cooling bath (Fisher Scientific) filled with
162 ethylene glycol cooling a 24/40 double-lumen coiled reflux tube (Ace Glassware, Vineland, NJ)
163 with a 500mL round bottom flask (Corning) heated with a heating mantle regulated by a timed
164 power controller (Glas-Col #O406 and #104A PL312, respectively).

165 Synthesis of ABP-dextran: The process of optimizing a bright, redshifted, pH-insensitive
166 fluorophore that is responsive to chloride concentration over a dynamic range inclusive of
167 expected extracellular chloride concentrations is beyond the scope of this paper and has been
168 published separately (Normoyle *et al.*, 2024). Synthesis techniques closely followed those of the
169 Verkman group when synthesizing related compounds (Verkman, 1990; Biwersi *et al.*, 1992)
170 and conjugating to dextran (Biwersi *et al.*, 1992). Briefly, N(4-***A***mino***B***utyl)***P***henantridinium
171 (ABP) was synthesized by a reflux of equimolar amounts of phenanthridine and N(4-
172 bromobutyl)phthalimide in acetonitrile followed by a second reflux in 6N HCl to hydrolyze
173 phthalate. Product was twice recrystallized from 95% ethanol before conjugation to cyanogen
174 bromide-activated 10,000g/moL (10KDa) dextran, producing 10KDa ABP-dextran with an
175 approximate molar labeling ratio of 4.4.

176 Sulfation of agarose: We modified the method of Fuse and Suzuki (Fuse & Toshiya, 1975) to
177 add sulfate groups to the repeating disaccharide units of agarose. The goal of maximizing
178 sulfation must be balanced with the consequent erosion of gel properties such as gelation and
179 water holding capacity; in our hands, the maximum sulfation we could achieve while retaining
180 gelation at 5% (w/v) was when using a 6:1 molar ratio of sulfuric acid to agarose disaccharide.
181 When cast at 5% (w/v), this worked out to ≈50mM sulfate in resultant gels (49.2+/-0.289mM; for
182 sulfate measurement see next section). This roughly matches calculated estimates of fixed
183 negative charges from a collection of bulk biochemical studies quantifying the content of sulfate
184 groups (proteoglycans and sulfatides) and carboxylic acid groups (sialic acid-bearing glycolipids
185 and proteins) in brain (Schnaar *et al.*, 2014). Schnaar et al. (2014) summarized the components
186 of the brain's extracellular matrix as follows: proteoglycans represent 0.45mM disaccharide
187 monovalent negative charge equivalents and sulfatides represent 5.8mM charge equivalents,
188 while sialic acid groups on gangliosides account for 3.9mM, and sialic acid bound to protein
189 comprises 1.3mM. In total, these distinct sources of extracellular negative charge bound to lipid,
190 protein, and sugar components of the extracellular matrix amount to 11.45mM sequestered into
191 the 20% of total volume that is extracellular. This gives a total expected fixed extracellular
192 anionic charge equivalent of 57.3mM in the brain's extracellular space. Proteoglycans, including
193 chondroitin sulfate, account for 2.3mM of total extracellular fixed charge (0.45mM corrected for
194 extracellular space being 20% of total). Despite this, we focus on chondroitin sulfate digestion of
195 live tissue due to experimental accessibility and the ability to use commercially available
196 chondroitinase. It is also for practical reasons that we model the complex extracellular matrix
197 using sulfated agarose because of the experimental expediency of adding sulfate to a
198 polymerizable sugar. We stress again that there is a limit to how much sulfate can be added to
199 agarose while retaining its ability to polymerize, and the following describes a sulfated agarose
200 with sulfate content near or at this limit. Briefly, agarose was added to a well-dried Erlenmeyer
201 flask and dissolved in DMSO at a concentration of 4%(w/v) at room temperature before being
202 cooled to 4°C with stirring. Addition of 4:1 mixture of acetic anhydride / glacial acetic acid, also
203 pre-chilled to 4°C, was added to agarose/DMSO mixture (0.4 volumes) in 4°C coldroom.
204 Vigorous mixing by handheld rotation was necessary to thin the gelatinous mixture to a slurry
205 and allow stirring at 4°C for 15 minutes; gentle heat transfer from experimenter's hands helped
206 loosen the initial gel but care is taken to return the mixture to 4°C. Sulfuric acid (15.6M) is then
207 added slowly at a 6:1 molar ratio to agarose repeating disaccharide units, taking care to keep
208 temperature between 4-10°C. Mixture is then moved to ambient temperature and allowed to stir
209 for 15 minutes before reaction is stopped by neutralization with 10M NaOH after again cooling
210 to 4°C and maintaining temperature between 4-10°C in coldroom. Sulfated agarose is then

211 dialyzed at ambient temperature in 12-14KDa dialysis tubing (SpectraPor S432703) against 15
212 volumes of 50mM Tris pH 7.4 once, then against distilled water changed twice daily until
213 dialysate clarifies. Agarose is then precipitated in 95% ethanol cooled to 4°C >4hours; over-
214 dialysis may hinder ethanol precipitation due to a lack of sufficient counter-ion presence.
215 Precipitate is then vacuum filtered and oven-dried at 50°C. Material is loosened with polished
216 glass pestle and stored at ambient temperature in sealed glass vial until use. Note that careful
217 temperature and pH control is necessary throughout exothermic processes to maintain gelation
218 characteristics of the product.

219 Measurement of sulfate concentration in polysaccharide gels: $BaCl_2$-gelatin turbidimetric method
220 (Torres *et al.*, 2021) was used to quantify the sulfate content of gel materials. Sulfated agarose
221 product or commercially available agarose or agar powder was dissolved in 0.5M HCl at a
222 concentration of 5% (w/v) in 2mL screw-top microtubes with gasket (Fisher Scientific). Tubes
223 are then placed in a heat block at 100-110°C for 3hours with periodic vortex mixing, hydrolyzing
224 the sugar backbone and releasing sulfate. All samples had varying amounts of insoluble dark
225 brown precipitated sugar, which was clarified at 20,000 x g for 10 minutes. Standards are
226 diluted from 1M Na_2SO_4 stock in 0.5M HCl. $BaCl_2$-gelatin reagent is freshly prepared by
227 dissolving 30mg gelatin in 10mL distilled water at 80°C for 10minutes, then promptly adding
228 100mg $BaCl_2$ and vortex mixing. $BaCl_2$-gelatin is then allowed to cool passively before use.
229 Samples are prepared by combining 1 part sample (diluted as desired), 1 part $BaCl_2$-gelatin,
230 and 3 parts 0.5M HCl. Assay is performed in a glass-bottom 96-well plate reading absorbance
231 at 405nm. Multiple sample dilutions were prepared and concentrations were calculated only
232 from dilutions whose readings were well within the dynamic range of the standards.

233 Measurement of Cl^- in agar or agarose gels (chemical method): Chloride was measured
234 colorimetrically using mercury(II) thiocyanate ($Hg(SCN)_2$) / iron(III) nitrate ($Fe(HNO_3)_3$)
235 absorbance method of Florence and Farrar (Florence & Farrar, 1971) to infer Cl^- from $Fe(SCN)_3$
236 production through the two-step reaction,

237 $$[\mathrm{Hg(SCN)_2} + 2\mathrm{Cl^-} \rightleftharpoons \mathrm{HgCl_2} + 2\mathrm{SCN^-}]\mathrm{x3}$$

238 $$[3\mathrm{SCN^-} + \mathrm{Fe(NO_3)_3} \rightleftharpoons \mathrm{Fe(SCN)_3} + 3(\mathrm{NO_3})^-]\mathrm{x2}$$

239 reading $Fe(SCN)_3$ absorbance at 490nm. Briefly, agar or agarose gels cast at 5% (w/v) in 3.5cm
240 Petri dishes were drained by gravity and then Kimwipes were used to gently wick away
241 remaining excess fluid at sides of dish. Similar amounts of each sample are transferred to 2mL
242 screw-top microtubes with gasket (Fisher Scientific) and 1 gel volume, estimated by weight, of
243 7.8M nitric acid (HNO_3) is added (final [HNO_3] = 3.9M). Samples are then placed in a heat block
244 at 100-110°C for 3hours with periodic vortex mixing, hydrolyzing the sugar backbone to break
245 down the gel lattice. All samples had varying amounts of insoluble dark brown precipitated
246 sugar, which was clarified at 20,000 x g for 10 minutes. A portion of supernatant or KCl
247 standard, diluted with 0.3M HNO_3, was combined with one-tenth volumes of 0.4M $Fe(NO_3)_3$ (in
248 4M nitric acid) and saturated $Hg(SCN)_2$ (in ethanol), triturated, and allowed 20minutes for
249 reaction to reach endpoint. Stock solutions are used within 1week. Multiple sample dilutions
250 were prepared and concentrations were calculated only from dilutions whose readings were well
251 within the dynamic range of the standards. Final concentrations are adjusted to account for
252 dilution from original gel sample volume.

253 Fluorescence Lifetime Imaging (FLIM): Time-correlated single-photon counting (TCSPC) FLIM
254 measurements were obtained using a custom laser-scanning two-photon rig driven by custom
255 ScanImage software (MBF Bioscience, Williston, VT) equipped with a MaiTai Ti:Sapph laser
256 (SpectraPhysics) and high-sensitivity PMT detectors (Hamamatsu C6438-01) as described
257 previously (Normoyle *et al.*, 2024). Briefly, ABP-dextran was excited at 760nm and emitted
258 photons were subjected to a 445/58 bandpass filter (Chroma) prior to detection using a high-
259 sensitivity PMT. ABP-dextran was used at 500microgram/mL (50μM) in aCSF unless otherwise
260 noted. A fluorescence lifetime is calculated for each pixel by measuring the time it takes for an
261 emitted photon to be detected, binning these photons according to arrival time, and to these
262 data a first-order exponential equation is fit to derive the rate constant representing the
263 fluorescence lifetime (Gehlen, 2020). The presence of a quencher will shorten fluorescence
264 lifetime to an extent which is linearly related to quencher concentration through the Stern-
265 Volmer equation,

266 $$\frac{\tau_o}{\tau_i} = 1 + [Q]k_{SV}$$

267 where τ_o / τ_i represents the unquenched lifetime divided by the shortened lifetime at a given
268 quencher concentration ([*Q*]) (Gehlen, 2020). The Stern-Volmer constant (k_{SV}) of the resultant
269 line relates the concentration of quencher to the shortening of fluorescence lifetime. Photons
270 were collected over an acquisition period of 60 seconds (*in vivo* and agarose gels) to 90
271 seconds (*in vitro* slice cultures) and the lag between incident laser pulse and resulting photon
272 detection recorded. The population of photons in each individual pixel is fit to an exponential to
273 yield a lifetime value and summed to yield an intensity value using the FLIMJ plug-in for ImageJ.
274 Further image processing, calculations, and statistics were accomplished using built-in functions
275 and custom routines developed in Matlab (v2018b and v2022a; Mathworks, Natick, MA). For
276 composite image generation, see *Image processing in Matlab* section below.

277 Calibration of ABP-dextran: ABP-dextran is synthesized, conjugated, and calibrated as
278 described previously (Normoyle *et al.*, 2024). Briefly, we calibrated 50μM ABP-dextran against
279 aCSF with varying chloride concentrations by preparing standard aCSF (in mM: NaCl 126; KCl
280 3.5; $CaCl_2$ 2; $MgCl_2$ 1.3; NaH_2PO4 1.2; Glucose 11; $NaHCO_3$ 15) and a low-chloride aCSF in
281 which NaCl was replaced with sodium gluconate. We mixed appropriate amounts of each to
282 vary chloride concentrations (10-136mM) while maintaining the sum of sodium chloride and
283 sodium gluconate at 136mM. Although k_{SV} values did not differ appreciably between ABP-
284 dextran batches nor when measured using different FLIM-capable microscopes, out of an
285 abundance of caution we used a single batch of ABP-dextran and obtained FLIM calibration
286 parameters specific for this batch of fluorophore and the custom microscope used for all
287 experiments reported in this manuscript. Because calibrations done in aCSF have a minimum
288 Cl^- of 10mM as described, the unquenched lifetime (τ_o) used for Stern-Volmer calculations is
289 approximated as the y-intercept (Cl^- = 0mM) of a best-fit curve of the raw calibration data;
290 empirically, a biexponential fit was used. Each concentration of Cl^- in the calibration curve has a
291 normally distributed set of ABP-dextran lifetime values with a near-constant relative standard
292 deviation (RSD = standard deviation divided by mean) (Normoyle *et al.*, 2024). All calculations
293 are otherwise done as described under *Fluorescence Lifetime Imaging (FLIM)* section above.

294 Animals: All animal protocols were approved by the Massachusetts General Hospital
295 Institutional Animal Care and Use Committee (protocol 2018N000221). Wild type mice (C57bl/6;
296 Jackson Labs 000664) of either sex were used for this study. Mouse pups remained in the

297 home cage with the dam under standard husbandry conditions until postnatal day 6 to 8 (P6–8)
298 when organotypic slice cultures were prepared, or until P26-30 when a cortical window was
299 surgically placed.

300 In vitro organotypic slice cultures and imaging: Organotypic hippocampal slice cultures were
301 prepared either as glass-mounted (Berdichevsky *et al.*, 2016) or membrane insert-mounted
302 (Stoppini *et al.*, 1991) cultures. Briefly, in either case hippocampi are obtained from P6-8 mice
303 and cut to 400μm thick slices. These are then gently transferred to a 6-well dish containing
304 either a membrane insert (Millipore) or a poly-L-lysine coated coverslip (Electron Microscopy
305 Sciences), are fed twice weekly with 1mL neurobasal-A media supplemented with 500μM
306 Glutamax, 2% B-27, and 0.03mg/mL gentamycin (all from Invitrogen), and are incubated at
307 35°C in a 5% CO_2 incubator. Cultures are typically imaged between DIV 12-21 in aCSF warmed
308 to 33°C and bubbled with 95%O_2 / 5% CO_2 perfused at a rate of approximately 100mL/hour
309 unless otherwise noted. Slices were pretreated with media containing 500μg/mL ABP-dextran in
310 incubator for 1-2 hours prior to perfusing with aCSF containing 136mM chloride and the same
311 concentration of ABP-dextran, plus 100nM tetrodotoxin (TTX). Slices were allowed to equilibrate
312 in perfusate for 20-30 minutes before imaging, equaling at least 2 hours of total exposure to
313 ABP-dextran prior to initiation of imaging. Two photon images were captured on a perfusion-
314 enabled stage with a 20x water-immersion objective, NA 0.95, and analyzed as described (see
315 *Image processing in Matlab* section below).

316 *In vivo* murine cortical window imaging: Using a modified method based on that of Che and De
317 Marco Garcia (Che & De Marco García, 2021), we placed cortical windows in young adult mice
318 (P26-30) for acute (non-survival) imaging in accordance with Massachusetts General Hospital
319 Institutional Animal Care and Use Committee policies and procedures (protocol 2018N000221).
320 Briefly, anaesthetized mice were immobilized with standard ear bars and nosepiece until custom
321 headbar is placed. A section of scalp is removed to expose a roughly 1cm section of skull.
322 Acrylic dental cement powder (Lang Dental, Wheeling IL) mixed with cyanoacrylate adhesive is
323 used to fix the headbar to the exposed skull at 4 o'clock to Bregma, creating a 5mm diameter
324 working area just lateral to midline. A 2.5mm round section of skull and underlying dura is
325 removed and a 3mm No. 1 coverslip is placed over the exposed cortex. Coverslip has 10μL
326 concentrated ABP-dextran / agarose mixture (1%w/v low gelation temperature agarose, Sigma-
327 Aldrich, with 10mg/mL ABP-dextran in aCSF) pipetted from 42°C heat block immediately before
328 inversion and placement over cortex. One hour is allowed before image acquisition for ABP-
329 dextran diffusion into cortex from overlying agarose (between cortex and coverslip), producing
330 signal similar to that seen with 50μM ABP-dextran in vitro. During this time the warmed
331 breadboard with immobilization apparatus and anesthetized mouse is transferred to the
332 microscope table for *in vivo* imaging. This custom-made gantry-type microscope accommodates
333 the breadboard as a stage for *in vivo* imaging. Two photon images were captured with a 16x
334 water-immersion long focal distance objective, NA 0.80, and were analyzed as described (see
335 *Image processing in Matlab* section below).

336 Agarose or agar gel Cl^- determination using ABP-dextran FLIM: Cl^- within an agar or agarose
337 gel was measured using the two-photon rig described above in the *in vivo* section, except with a
338 4x (NA 0.28) objective. Using an 8-well microchamber with silicone dividing gasket (Ibidi,
339 Grafelfing, Germany), gels were cast in aCSF containing ABP-dextran and subsequently
340 transferred to a single Petri dish where they were equilibrated with aCSF containing ABP-
341 dextran for at least 1 hour prior to imaging. FLIM measurements were taken as described,

342 generally one field per quadrant at a depth of between 50-100microns. Importantly, the gasket
343 separating gels of differing compositions was removed such that all gels in an experiment were
344 bathed in the same aCSF with the same Cl^-. Where gels were kept for more than 1 day, they
345 were prepared in aCSF without glucose and kept refrigerated between readings to prevent
346 fouling.

347 Chondroitinase treatment of organotypic hippocampal slice cultures: Chondroitinase ABC
348 (ChABC; AMSBIO, #E1028-02) was brought up in aCSF containing 0.1% bovine serum albumin
349 (BSA) to a concentration of 1U/mL. Slices grown on membrane inserts were treated for 1hour
350 either with aCSF containing ChABC or sham aCSF containing only the 0.1% BSA vehicle. Both
351 experiment and control had 0.5mg/mL ABP-dextran (50μM), and FLIM imaging was done using
352 the two-photon rig described in the *in vivo* section above. At the conclusion of imaging, the
353 aCSF was collected for detection of liberated chondroitin sulfate.

354 Measurement of sulfated glycosamioglycans (sGAGs) liberated in aCSF: Blyscan 1,9-
355 dimethylmethylene blue-based kit (Biocolor, #B1000) was utilized for measurement of sGAGs
356 including chondroitin sulfate proteoglycans (CSPGs). After treatment with aCSF containing
357 ChABC or BSA vehicle as detailed above, aCSF was collected and measured as directed
358 against standards of bovine trachea chondroitin (Blyscan kit standard) with appropriate amounts
359 of 10x stocks of aCSF and 0.1% BSA to obtain concentrations identical to samples. 1,9-
360 Dimethylmethylene blue reagent absorbance is read at 650nm.

361 Measurement of chondroitin sulfate by liquid chromatography / mass spectroscopy (LC-MS):
362 aCSF containing either chondroitinase or vehicle was recovered after incubation with slice (see
363 above), volume recovered carefully noted before freezing at -20˚C, and shipped over dry ice
364 with blinded labels for analysis. The samples were filtered using 3K MWCO spin filter units (Pall
365 Corporation Nanosep with 3K Omega Ref: OD003C34) at 14000 RPM at 10˚C for 20minutes.
366 The flow through containing CS disaccharides was dried in speed vac. The dried flow through
367 were reconstituted in 200μl ultrapure distilled water (Invitrogen, Cat # 10977-015) and 100μl
368 was dried taken for $^{12}C_6$ aniline tagging by reductive amination method (Lawrence *et al.*, 2008).
369 Briefly, the CS disaccharides were dissolved in 17μl of $^{12}C_6$ aniline followed by addition of equal
370 volume of freshly prepared 1 M $NaCNBH_3$ (Sigma-Aldrich) in dimethyl sulfoxide: acetic acid
371 mixture (65:35, v/v). The reaction mixture was kept at 70°C for 45min and then transferred to
372 dry oven at 37°C for overnight reaction (16 h). After aniline tagging samples were dried in
373 speed-vac for 48h to remove excess reagents. The samples were then dissolved in 17μL of LC-
374 MS grade water (Honeywell), centrifuged at 7000g for 5min. 5μL of the sample was taken and
375 mixed with 5μL reconstitution buffer containing known amount of internal standard (5μl of the
376 reconstitution buffer contains, 1 μl of 10X LC-MS buffer-A (80 mM acetic acid and 50 mM
377 dibutylamine; Sigma-Aldrich), 2 μl of $^{13}C_6$ aniline-tagged CS disaccharide internal standard
378 mixture (20pmole each) and 2 μl LC-MS grade water. CS disaccharides were analyzed by LTQ
379 Orbitrap Discovery (Thermo Scientific) mass spectrometry attached with liquid chromatography
380 system (Ultimate3000, Thermo-Dionex). All disaccharides were separated on a reverse phase
381 C18 column (1mm x 150mm, 5μm, Targa, Higgins Analytical) using buffer containing dibutyl
382 amine as ion-pairing reagent, followed by detection of disaccharides on mass spectrometer in
383 negative ionization mode. The chromatographic steps were: 100% buffer-A (8mM acetic acid,
384 5mM DBA) for 10 min followed by stepwise increase of buffer-B amount; 17% buffer-B (70%
385 methanol, 8 mM acetic acid, 5 mM DBA) for 10 min; 32% buffer B for 15 min; 40% buffer B for

386 15 min; 50% buffer B for 15min; 60% buffer B for 15 min; and 100% buffer A for 10 min. Flow
387 rate was kept at 50µL per min.

388 Calculation of ECM sulfate lost after chondroitinase digestion: In order to contextualize the Cl^-_o
389 increase we observe after chondroitinase treatment of OHSCs, we used our HPLC-derived data
390 and approximated OHSC volume to derive a reasonable expected Cl^-_o value for comparison.
391 HPLC data was obtained from collected chondroitinase (or sham) digestion aCSF of a known
392 volume. Chondroitin disaccharide concentration and sulfate content were found analytically, and
393 a total chondroitin and total sulfate amount were calculated from mean values of chondroitin
394 sulfate content (0.2mg/mL), sample volume (0.725mL), sulfation ratio (0.95 sulfate per
395 disaccharide), and a monosulfated disaccharide molar mass of 481.4g/moL. Given mean OHSC
396 thickness of 266µm and typical OHSC dimensions of 3x1.5mm, we calculate the best
397 approximation of extracellular volume (20% of total slice volume) to be 0.293mL. The organic
398 sulfate content lost from total ECS volume comes out to 1.65mM when assuming full-depth
399 uniform chondroitinase digestion, or 8.8mM assuming depth-dependent digestion affecting only
400 50µm nearest the chondroitinase reservoir (i.e., nearest the perfusate). For comparison to
401 measured Cl^-_o, we assume the molar relationship between sulfate lost and chloride gained to be
402 1:1.

403 Image processing in Matlab: ABP-dextran fluorescence lifetime is converted to Cl^-_o as described
404 above. Composite Cl^-_o images, depicting Cl^-_o values via colormap while incorporating structural
405 data through brightness adjustment, were produced using custom Matlab routines that apply
406 normalized intensity data to Cl^-_o images in a manner similar to commercial FLIM software. Note
407 that intensity images were generated by summation of photons for each pixel across 32 time
408 bins after excitation, resulting in a higher intensity background than is typical in standard two-
409 photon images.

410 *Pixel exclusion*: We sought to perform as little processing of either intensity or lifetime data as
411 possible, using statistical methods to objectively exclude pixels greater than three standard
412 deviations from the mean of either property. Any remaining pixels reflecting a fluorescence
413 lifetime outside the calibrated range (0-150mM Cl^-), as happens in pixels with poor data quality
414 typically due to low signal, were also excluded. More specifically, pixels were excluded if ABP-
415 dextran lifetimes were in excess of the mean at 0mM chloride, or if lifetimes were shorter than
416 twice the standard deviation less than the mean at 150mM (calculated from calibration data).
417 This yielded total objective exclusion of 0.1-0.5% of pixels in a given image, which were set to
418 black. Subjective exclusions were done either by manually drawn regions of interest (ROI) to
419 exclude areas of perfusate at the margins of OHSCs or large blood vessels *in vivo*, or else by
420 image-specific thresholding to exclude low-intensity areas coinciding with apparent somatic
421 silhouettes. All exclusions were performed prior to analysis of extracellular Cl^-_o. To ensure that
422 somatic silhouette-defined pixels, in particular, were not a subpopulation of pixels possibly
423 reflecting ABP-dextran in an atypical compartment (e.g., the intracellular space), multiple
424 analyses of excluded versus included pixels were performed to confirm faithful extracellular
425 ABP-dextran signal and appropriateness of pixel exclusion (see Results).

426 *Neuronal tracing analysis:* Where somatic borders were traced for analysis, these were not
427 dependent upon thresholding but were traced manually where neurons within the focal plane
428 could be confidently identified based upon morphology. Traces followed the exterior aspect of
429 the visually apparent border between bright and dim signal (see Results). Data was linearized
430 and is presented as the pixelwise change in Cl^-_o versus linearized distance, the latter calculated

from pixel centerpoints. Comparison control data is derived by applying the same traces over calibration solution images, in which stochastic pixel to pixel differences are isolated (e.g., machine noise, Brownian motion artifact, etc). *In vivo* analysis was optimized for more superficial L1 cortical imaging and demonstration of ABP-dextran exclusion from vasculature and intracellular space, but a limited number of L2/3 neurons were also identified *post hoc* by their silhouettes formed through ABP-dextran exclusion within deeper fields. Morphological identification at this suboptimal optical zoom was only possible where pyramidal neurons were well within the chosen focal plane, producing demonstrably pyramidal silhouettes. This yielded a limited dataset on which we repeated perineuronal tracing analysis as an initial *in vivo* conformation of our better-optimized *in vitro* studies.

Regions of interest (ROIs) selection: ROIs are defined using intensity images for OHSCs either as a differentiation between tissue and surrounding bath, or this plus a regular division of the field (i.e., quarters or eighths) as indicated. ROI fields containing a majority of excluded pixels (e.g., perfusate) are excluded from analysis. ROIs are defined *in vivo* as cortical regions between anatomical landmarks, such as large vessels, which are easily identified through their exclusion of ABP-dextran. ROIs are then converted to masks and applied to fluorescence lifetime or Cl^-_o images. ROIs in fields in which somatic silhouettes are evident are distinguished from ROIs that are too superficial to contain discernable silhouettes such as cellular (Layer 2/3) or acellular (Layer 1) cortical fields, respectively.

Statistics: Statistical analysis was done with Matlab 2022a, with access to statistical toolbox functions. Individual tests used and *p*-values are detailed in figure legends. Corresponding *p*-value levels are indicated within figures by asterisks and listed in figure legends. Where sample sizes are small, we first determined whether we could assume normal distributions using the Jarque-Bera test (Matlab built-in function jbtest); where non-parametric tests were required, we utilized Mann-Whitney ranked sum or Kolmogorov-Smirnov tests as noted. *In vivo* statistical analysis of cortical Cl^-_o was accomplished with ROI mean values, but because ROI size and number varies between groups we report mean+/-standard deviation of all analyzed pixels in addition to the ROI mean+/-standard error associated with ANOVA analysis. In the interest of transparency we elected to display violin plots of all pixels analyzed overlaid with ROI mean+/-standard error, using ANOVA analysis of the latter to determine significance of findings.

Data availability statement: All data files used to generate the figures in the paper can be found on GitHub under KieranNormoyle/NeuronalChloride2023.

Results

Non-invasive measurement of extracellular chloride using ABP-dextran: ABP is a novel Cl-sensitive fluorophore compatible with Fluorescence Lifetime IMaging (FLIM) that we have optimized to be bright, red-shifted, and sensitive to chloride concentrations through the range that would be encountered in in the extracellular space. We conjugated ABP to a 10,000 Dalton (10KDa) dextran resulting in an amine-bonded moiety (Figure 1A) that is resistant to pH changes in the physiological range (Normoyle *et al.*, 2024) and is restricted to the extracellular space (see below). We validated the ability of ABP-dextran to reliably report chloride concentration by correlating the shortening of ABP-dextran fluorescence lifetime to chloride concentration (Figure 1B) through the Stern-Volmer relationship (Figure 1C), generating a k_{SV} of $15.9M^{-1}$ for ABP-dextran used in these experiments. The fluorescence lifetime of ABP-dextran is not dependent upon the concentration of ABP-dextran, only the concentration of chloride.

475 Chloride concentration also affects ABP-dextran intensity, such that high chloride
476 concentrations not only shorten the emission lifetime but also reduce the intensity of emission.
477 However, the concentration of chloride can be calculated (independently of the local ABP-
478 dextran concentration) as long as sufficient photons are collected to calculate fluorescence
479 lifetime in a given pixel.

480 Sulfated agarose gels as an *in vitro* model of perineuronal space: We recently observed that
481 differing concentrations of chloride juxtaposed to one another were stable on time scales of at
482 least 100 minutes due to the presence of immobile anionic charges present in the neuronal
483 cytoplasm (Rahmati *et al.*, 2021), an effect known as Donnan exclusion (Marinsky, 1985;
484 Helfferich, 1995; Fatin-Rouge *et al.*, 2003; Epsztein *et al.*, 2018; Gao *et al.*, 2022). We tested
485 whether Donnan exclusion was also operative in the extracellular space as a consequence of
486 the abundant fixed negative charges present on extracellular glycolipids and glycoproteins
487 (Schnaar *et al.*, 2014), focusing in particular on the sulfate moieties of the glycosaminoglycans
488 that comprise the bulk of the extracellular matrix in the brain (Karamanos *et al.*, 2021). This
489 matrix is most frequently visualized as the perineuronal lattice-like structures around all neurons
490 and first described by Golgi in 1898 (Golgi, 1898; Celio *et al.*, 1998). More recently the term
491 'perineuronal nets' has been applied to a specific extracellular structural motif associated with
492 some interneurons and recognized by specific agents such as *wisteria floribunda* agglutinin
493 (WFA); however, perineuronal space contains a ubiquitous, if variable (Deepa *et al.*, 2006),
494 abundance of negatively charged moieties (Schnaar *et al.*, 2014) and Donnan exclusionary
495 effects remain ubiquitous even as specific perineuronal environments vary among neuron
496 subtypes. The process of Donnan exclusion does not require an ongoing energy input, although
497 this issue has been contested (Glykys *et al.*, 2014b; Voipio *et al.*, 2014). We therefore modeled
498 the brain's extracellular matrix using a reduced system to remove the possibility of active
499 buffering of Cl^-_o by astrocytes (Egawa *et al.*, 2013) or other cellular or vascular elements. We
500 used gels of sulfated agarose to mimic the sulfated glycosaminoglycans such as the chondroitin
501 sulfate-decorated aggrecan family members that are prominent in the perineuronal matrix.
502 Agarose is a nominally sulfate-free linear glycopolymer that is a major component of agar
503 (Figure 2B; bars 1 and 2) that was used as a chemically homogenous starting material for
504 covalent sulfate linkage. We optimized the method of Fuse and Suzuki (Fuse & Toshiya, 1975)
505 to balance the gelatinizing properties of agarose with the dispersive, hydrophilic Donnan effects
506 arising from incorporation of the charged sulfate groups (Gregor, 1951; Helfferich, 1995). We
507 obtained a sulfated agarose that could be used to cast gels with 50 mM effective sulfate
508 concentration (Figure 2B, bar 3; 49.8+/-0.9mM sulfate across three batches [mean+/-SD])
509 covalently linked to the polymerized agarose lattice. Gels cast from sulfated agarose serve as a
510 simple *in vitro* model of the perineuronal extracellular space, allowing us to investigate the ability
511 of covalently linked anions attached to a three-dimensional matrix to displace mobile chloride
512 ions.

513 We measured the chloride concentrations within non-sulfated agarose gels vs. sulfated agarose
514 gels, each equilibrated in aCSF, and compared these to the chloride concentration in the
515 surrounding aCSF using either a standard colorimetric iron(III) thiocyanate assay (Figure 2C,
516 dark gray bars) or ABP-dextran FLIM imaging (Figure 2C, light gray bars). Agarose gels with
517 fixed anions in the form of covalently bound sulfate had significantly decreased chloride
518 concentrations versus both control aCSF and non-sulfated agarose gels (Figure 2C, right pair vs
519 left and center pairs, respectively) measured either with the standard chemical assay (dark gray
520 bars; p = 0.00264 and p = 0.00354 by Student's paired t-test, respectively) or ABP-dextran FLIM

521 (light gray bars; $p < 0.001$ by Student's paired *t*-test for either comparison). We measured a
522 small chloride increase within non-sulfated agarose gels vs control aCSF in either assay,
523 representing an insignificant increase when using the standard chemical assay (8.05+/-6.14mM,
524 mean+/-standard deviation; $p = 0.190$ by Student's paired *t*-test) and a smaller yet statistically
525 significant increase when measured using ABP-dextran FLIM (4.95+/-0.51mM, mean+/-
526 standard deviation; $p = 0.00328$ by Student's paired *t*-test). Later ABP-dextran FLIM
527 experiments comparing aCSF perfusate to non-sulfated gels show no such difference (see
528 below and Figure 2E). This Cl^- increase is curious but is quantitatively small and qualitatively
529 distinct from the Cl^- decrease we see in sulfated agarose gels (3.5% increase from non-sulfated
530 gel vs. aCSF control compared to a 40.7% decrease from sulfated agarose gel vs. aCSF
531 control, respectively), meaning that any effect would be a small overestimation of Cl^- within
532 sulfated agarose gels. The overall agreement of results derived from both assays lends
533 confidence to the reliable performance of ABP-dextran FLIM versus standard chemical
534 colorimetric methods of Cl^- measurement.

535 Next we placed separately cast non-sulfated and sulfated gels adjacent to each other and
536 equilibrated in the same aCSF bath with ABP-dextran (Figure 2D; schematic in Figure 2A).
537 ABP-dextran FLIM measurements of chloride concentration within the non-sulfated and sulfated
538 gels demonstrated significant chloride concentration differences between gels that had no fixed
539 anionic charge to displace mobile chloride (non-sulfated agarose; Figure 2D light blue bars) vs.
540 gels that had covalently bound sulfate groups (sulfated agarose; Figure 2D dark blue bars). The
541 chloride concentrations were inversely proportional to the sulfate concentration in the gel, were
542 significantly lower for sulfated gels at each time point (each $p < 0.001$), and were stable for over
543 three weeks (agarose gel comparisons: each $p = 1.0000$; sulfate gel comparisons: 2-4hours vs
544 24hours $p = 1.0000$, 3weeks vs 2-4 hours and 24 hours $p = 0.211$ and $p = 0.113$, respectively;
545 ANOVA with Bonferroni correction). These findings support the displacement of mobile chloride
546 ions by the sulfates fixed to the gel (Figure 2D) by Donnan exclusion. We next imaged both non-
547 sulfated and sulfated gels immediately juxtaposed to one another, along with aCSF perfusate, in
548 the same field (Figure 2E) and demonstrated that the presence of sulfate groups covalently
549 bound within the polymerized gel results in a significantly decreased chloride concentration
550 relative to both non-sulfated gels and aCSF perfusate (Figure 2E, bar 3 vs bar 2 and bar 1,
551 respectively; each $p < 0.001$ by Student's paired *t*-test). Non-sulfated agarose gels
552 demonstrated no difference versus aCSF perfusate ($p = 0.0647$ by Student's paired *t*-test).

553 <u>Demonstration of chloride displacement in living systems:</u> To test whether Donnan exclusion is
554 also operative in the extracellular matrix of the brain, we studied mouse hippocampal
555 organotypic slice cultures. We tested whether extracellular perineuronal fixed anions, such as
556 the chondroitin sulfate moieties of aggrecan family proteoglycans (Frantz *et al.*, 2010;
557 Karamanos *et al.*, 2021), displace chloride in this living system. After incubation with ABP-
558 dextran and equilibration with aCSF containing ABP-dextran and 136mM chloride, we measured
559 extracellular chloride concentration using ABP-dextran FLIM and found that Cl^-_o was
560 unexpectedly low and heterogenous (46.7 +/- 18.8 mM, calculated from 25.8×10^6 pixels across
561 32 fields of 7 slices). Representative fields are shown in Figure 3A (ABP-dextran intensity) and
562 Figure 3B (Cl^-_o composite image, quantified in Figure 3C). Paired analysis of slices pre- and
563 post-ABP-dextran incubation confirmed that autofluorescence signals in pixels in pre-ABP
564 images did not contribute to the unexpectedly low values of Cl^-_o obtained from post-ABP
565 images. This is because pre-ABP pixels that had both sufficient photon count to allow lifetime

566 calculation and lifetimes within the calibrated range of ABP-dextran had short lifetimes whose
567 effect would be to increase the reported Cl^-_o, not decrease it.

568 Perineuronal traces along the outer edge of neuronal silhouettes (Figure 3B, white dashes)
569 were used to analyze the spatial change in Cl^-_o in the extracellular space immediately adjacent
570 to the neuronal cytoplasmic membrane. Pyramidal neuron silhouettes were identified
571 morphologically and pixels underlying the extracellular margin (i.e., perineuronal) traces were
572 linearized for analysis. We compared the size of the effects of fixed anions on local Cl^-_o to
573 Brownian and machine noise arising from FLIM of ABP-dextran in bulk solutions with similar
574 mean Cl^-_o. The pixel-to-pixel change in Cl^-_o (ΔCl^-_o) versus distance in the presence of fixed
575 anions in the perineuronal space (Figure 3D, blue) was much larger than the ΔCl^-_o versus
576 distance in the absence of fixed anions in bulk solution containing ABP-dextran and a single
577 concentration of Cl^- (Figure 3D, red). Figure 3E shows similar data for a larger cohort of
578 perineuronal tracings and their corresponding aCSF solution counterparts (72 neurons traced
579 from 6 OHSCs). We found a consistently increased probability of greater ΔCl^-_o per micron in the
580 extracellular space where fixed extracellular anions were present compared to the perfusate
581 aCSF (Figure 3E, blue vs red).

582 We further analyzed dim pixels typical of the neuronal silhouettes, which had not already been
583 statistically excluded and displayed as black. These dim pixels retain their Cl^-_o colormap values
584 but are often so dim they are difficult to appreciate visually (e.g., Figure 3B). They are included
585 in presented images in the interest of transparency but were excluded from Cl^-_o analysis after
586 applying an empirically derived threshold value that best approximates the clearest silhouettes
587 in each image. We reasoned that these pixels represented photons originating from extracellular
588 ABP-dextran above or below the focal plane, likely present due to the higher-background FLIM-
589 derived intensity images (Figure 4A) which represent a summation of all photons in each pixel.
590 Because Cl^-_o is derived from the intrinsic, intensity-independent property of fluorescence
591 lifetime, structural context is lost in Cl^-_o images (Figure 4B) and must be reestablished by
592 incorporation of intensity information into a composite image (Figure 4C). This is not unique to
593 Cl imaging; commercial FLIM software creates intensity-lifetime composite images in a similar
594 manner. In our images we first converted from fluorescence lifetime to Cl^-_o to allow the use of a
595 linear colormap for readers' ease of interpretation (see Methods).

596 The dim, excluded pixels occurring in neuronal silhouettes offered an opportunity to assess
597 whether they were in fact caused by out-of-focus extracellular ABP-dextran, consistent with
598 recent super-resolution imaging of the extracellular space utilizing a 10KDa dextran-linked
599 fluorophore in addition to unconjugated fluorophore (Tønnesen *et al.*, 2018). If true, this would
600 produce a similar, if wider (Normoyle *et al.*, 2024), distribution of Cl^-_o values. Conversely, if the
601 dim, excluded pixels were autofluorescent in origin or were reflective of low Cl^-_i reported by
602 ABP-dextran leaked into neurons, then we would find a right-shifted, high-Cl^-_o distribution or a
603 left-shifted, low-Cl^-_o distribution, respectively.

604 <u>Verification of ABP-dextran extracellular compartmentalization:</u> We used two approaches to
605 assess the Cl values reported in the dimmest pixels. We first compared all pixels below the
606 exclusion threshold to all pixels above the threshold. Only pixels outside the actual slice (i.e.,
607 perfusate pixels) and those pixels with lifetimes outside the calibrated range of ABP-dextran
608 were not considered. We found that included and excluded pixels had histograms with similar
609 characteristics, such as mean and mode, although excluded pixels were fewer in number and
610 had a wider distribution (Figure 4D, blue vs gray). There is neither a high-Cl^-_o peak indicative of

611 autofluorescence nor is there a low-Cl^-_o peak indicative of intracellular signal in either included
612 pixels or excluded pixels. Notably, there are virtually no included pixels in the typically
613 intracellular range (i.e., ≤15mM Cl^-), and such pixels are far more likely to be excluded from
614 analysis (Figure 4D, gray arrow). We conclude that intensity-excluded pixels are not a low- or
615 high-Cl^-_o subset, which would seem to preclude errant Cl^-_i signal. However, we wanted to rule
616 out any possible non-extracellular signal more specifically as most pixels at these resolutions
617 are expected to contain a portion of both neuropil and extracellular space.

618 As a second means to evaluate the Cl values reported in the dimmest pixels, we assessed
619 pixels within individual somatic silhouettes. Visually apparent somatic edges are ideal to
620 compare extracellular ABP-dextran signal in the bright perineuronal exterior of silhouettes to
621 ostensibly intracellular pixels inside the silhouette margins. The fact that the brightest of these
622 pixels are located nearest the outer silhouette margin and the least intense pixels are located
623 toward silhouette centers supports our hypothesis that this signal is extracellular in origin from
624 outside the focal plane. Alternatively, if ABP-dextran leaked inside cells, despite its conjugation
625 to 10KDa dextran, we would expect that such an intracellular signal would be brightest in the
626 silhouettes formed by cells firmly within the focal plane (i.e., with the most ABP-containing
627 cytoplasm in the focal plane). After the objective pixel exclusion step (intensity greater than
628 three standard deviations from the mean, or lifetime outside the calibrated range), we compared
629 Cl^-_o in the perineuronal margin within one micron external to the traced border to those pixels
630 inside the traced border. In this way our analysis was restricted to only those cells
631 morphologically identified as pyramidal neurons adequately centered in the focal plane. Pixels
632 from inside the silhouette are greater in number than perineuronal extracellular pixels in this
633 analysis, yet we saw no subpopulation of intracellular chloride values (i.e., in the range of 15mM
634 Cl^-) that would be expected if this signal were originating from 'leaked' intracellular ABP-dextran
635 (Figure 4E). Signal from the one micron external to the perineuronal perimeter is five times as
636 bright on average as pixels from within the silhouette (Figure 4F), which helps explain why the
637 excluded intracellular signal has a wider distribution of Cl^-_o values (Normoyle *et al.*, 2024). If no
638 intracellular leakage of ABP-dextran can be detected even within in-focus neuronal somatic
639 silhouettes, where such signal is expected to be strongest if it were present, one can infer that
640 neuropil will not contribute any such signal in pixels containing both neuropil and extracellular
641 space. While we look forward to future experiments with greater spatial resolution, we conclude
642 that neither objectively excluded pixels nor those excluded by intensity thresholding are
643 indicative of low- or high-Cl^-_o subsets. Further, we provide ample evidence supporting the fidelity
644 of ABP-dextran in its reporting of chloride exclusively in the extracellular space.

645 <u>Demonstration of chloride displacement by chondroitin sulfate:</u> We then confirmed that fixed
646 anions, including chondroitin sulfate glycoproteins, are a significant contributor to the observed
647 difference between expected and measured Cl^-_o by measuring Cl^-_o before and after treatment
648 with chondroitinase. Analogous to matrix metalloproteases, chondroitinase is a bacterial
649 enzyme that cleaves the sulfated glycopolymer chondroitin. Chondroitinase treatment
650 significantly increased Cl^-_o in organotypic hippocampal slice cultures (Figure 5A&B; pre- and
651 post-digestion, respectively). Cl^-_o increased on average 8.3+/-3.3mM (mean+/-standard
652 deviation) in freely diffusible extracellular chloride within the slice culture (Figure 5A vs 5B;
653 quantified in 5D-F) and was significantly greater in chondroitinase digested slices than in sham
654 digested slices (Figure 5B vs 5C; quantified in 5F). This increase in Cl^-_o coincides with a
655 significant decrease in the extracellular fixed anions within the slice culture. While chondroitin
656 sulfate is targeted in this experiment, proteoglycans collectively make up less than 10% of the

657 extracellular fixed charge; gangliosides and sulfatides make up the balance (Schnaar *et al.*,
658 2014). The actual decrease in fixed anion concentration in the extracellular space was
659 estimated from the concentration of chondroitin sulfate released into the perfusate after
660 chondroitinase treatment (Figure 5G) and confirmed by HPLC analysis (Figure 5H). Quantitative
661 estimates of fixed anionic charge in the perineuronal space are few in the absence of a
662 quantitative fluorescent or histological sensor. Those present in the literature are either based
663 on novel techniques (Marinsky, 1985) or else are extrapolated from non-neuronal tissues also
664 rich in chondroitin sulfate (Urban *et al.*, 1979; Chahine *et al.*, 2005). We estimated the expected
665 Cl^-_o increase after chondroitinase digestion using HPLC-derived measurements of released
666 chondroitin disaccharides and OHSC volume (see Methods). Careful *in vitro* studies of
667 chondroitinase have concluded that only approximately 50% of total chondroitin sulfate is
668 accessible to chondroitinase (Lin *et al.*, 2008). This is likely not due to a diffusion restriction
669 (Hrabetová *et al.*, 2009) and more likely is related to enzyme activity, perhaps due to variance in
670 local matrix structures. Our own empirical observations in OHSCs, in agreement with others'
671 published observations (e.g. Orlando and colleagues, especially Figure 5C therein) (Orlando *et*
672 *al.*, 2012) indicate that chondroitinase activity decreases with distance from its diffusive
673 reservoir and full activity is restricted to an estimated 50μm; as such we only measure Cl^-_o to a
674 depth of 50μm. Rather than seek definitive conclusions about the enzymatic efficiency of
675 chondroitinase at this time, we performed calculations for each case. If all digested chondroitin
676 sulfate indeed came from only the most superficial 50μm of our OHSCs, the Cl^-_o increase
677 expected in this same superficial 50μm is calculated to be 8.8mM (see Methods). This agrees
678 well with experimental mean Cl^-_o values calculated from regular subfields of pre- and post-
679 chondroitinase digestion, 8.8mM versus 8.3+/-3.3mM (Figure 5E), or when using the full field to
680 calculate the minimum and maximum range of Cl^-_o increases from 0.6-16.1mM (Figure 5D; pre-
681 digestion mean minus standard deviation to post-digestion mean plus standard deviation).
682 Further, we find that even if we assume chondroitin sulfate is lost uniformly from the full
683 thickness of the OHSC and recalculate a smaller expected Cl^-_o increase of 1.65mM, this still lies
684 within the empirically measured range of 0.6-16.1mM. These observations are consistent with
685 the expected inverse relationship between fixed extracellular anions such as sulfate and mobile
686 Cl arising from Donnan exclusion. They are also consistent with the fact that chondroitin sulfate,
687 while experimentally accessible, only accounts for a minority of total expected perineuronal fixed
688 anionic charge despite being the dominant sGAG in the perineuronal space. Estimations
689 employing bulk biochemical measurements from rat brain (Schnaar *et al.*, 2014) suggest that
690 the actual fixed anionic charge contribution from chondroitin sulfate is approximately 2mM
691 equivalent charge (see Methods) in agreement with our findings and consistent with the
692 electrophysiological findings of others (Klein *et al.*, 2018). It would be advantageous to similarly
693 estimate a predicted Cl^-_o based upon local sulfate concentrations and compare this to empirical
694 Cl^-_o measurements similar to our sulfated agarose experiments (Figure 2E), but without direct
695 and independent measurement of the extracellular sulfate content of OHSCs this is not currently
696 feasible. In summary, the immobile ions associated with the extracellular matrix displace mobile
697 anions such as chloride consistent with the well-established effects of Donnan equilibrium
698 forces, such that Cl^-_o is much lower and less uniform than would otherwise be expected.

699 <u>Chloride displacement in the perineuronal space *in vivo*</u>: To test whether Donnan exclusion of
700 Cl^-_o by sulfated GAGs and other fixed anions was significant *in vivo*, we performed live 2 photon
701 imaging of P26-30 mice via a cortical window (Figure 6A). Direct application of high
702 concentrations of ABP-dextran into the non-sulfated agarose overlying the neocortex (Figure

6B) resulted in a robust ABP fluorescence signal from the extracellular space of the brain parenchyma, similar in intensity to 50μM ABP-dextran used *in vitro*. Control measurements were obtained from the agarose above the cortex, which had been brought up in aCSF (136mM Cl^-) and allowed to equilibrate with *in vivo* CSF. Notable exclusion of ABP-dextran fluorescence emission from blood vessels (Figure 6C,D&E) and cell bodies (Figure 6D) was observed. Areas of locally elevated Cl^-_o and overall bright signal seen in OHSCs (Figures 3-5) were absent *in vivo* (Figure 6), suggesting these features are specific to *in vitro* preparations. At several microns in size, we reason the areas seen in OHSCs are most likely damaged areas where intracellular space makes up less than the typical 80% of volume allowing ABP-dextran access to a greater proportion of volume, so that the signal is bright despite quenching by the high Cl^-_o in these spaces. ECM damage would also be likely in such circumstances and would be expected to result in a loss of extracellular immobile anions, limiting the Donnan exclusionary force and leading to relatively high concentrations of Cl^-_o. This combination would be expected to result in a paradoxically bright, short-lifetime ABP-dextran signal yielding an unusually intense high Cl^-_o area. Given the absence of these features *in vivo*, we speculate that these areas are the result of slicing trauma but longitudinal studies will be needed to adequately categorize them. Regions of interest (ROIs) were defined using intensity images before rendering composite images so that only structural information was considered; an example intensity and composite image pair can be seen in Figure 6C&E. Perineuronal tracing analysis was repeated for the limited number of layer 2/3 neurons we could identify by morphology and confirmed that perineuronal $\Delta[Cl^-]_o$ per micron *in vivo* is similar to *in vitro* findings (Figure 6D inset, F&G; compare to Figure 3D&E). Cortical Cl^-_o was less than half the chloride concentration measured in the overlying agarose (48.1 +/- 17.0mM, calculated from 68 ROIs and 4 animals, versus 135.4 +/- 5.0mM in agarose between cortex and coverglass). Cl^-_o in cellular and acellular fields displayed in Figure 6C,D&F were not significantly different from each other (Figure 6E entries 2&3, respectively), nor were either significantly different from all ROIs collected from this animal (entry 4) or from all animals (entry 5; each $p = 1.0000$ by ANOVA with Bonferroni correction), while all were significantly different when compared to aCSF measured above the cortex (each $p < 0.001$ by ANOVA with Bonferroni correction). Regional mean Cl^-_o values were approximately 45-55mM (Figure 6E) but there was notable spatial variation between regions and even within regions, similar to *in vitro* OHSC results and consistent with local Donnan exclusion of Cl^-_o by local variation in fixed anions such as sulfated GAGs. Future experiments will be optimized for higher resolution imaging, but our results suggest that the well-established heterogeneity of sulfation patterns around neurons represent a means by which neurons and supporting cells can indirectly modulate Cl^-_o through Donnan forces in a manner similar to how cytoskeletal components, in particular actin, have been recently shown to influence local intracellular Cl^-_i (Rahmati *et al.*, 2021).

Discussion

We demonstrate stable Donnan exclusion of chloride by fixed anions in a transport-free system of sulfated agar using FLIM of a novel fluorophore, ABP-dextran, and validate these measurements with direct chemical assays of sulfate and chloride (Figure 2). FLIM of ABP-dextran demonstrated that Cl^-_o in the brain is less than half the Cl concentration in the cerebrospinal fluid and plasma (Figures 3-6). This low Cl^-_o arises from Donnan exclusion of chloride by fixed anions including sulfated glycosaminoglycans (sGAGs), because release of sGAGs by chondroitinase results in an increase in Cl^-_o that varies with the amount of sulfates released (Figure 5). Major findings are confirmed *in vivo* (Figure 6).

749 Limitations of this study

750 The finding that Cl^-_o is much lower than expected in the extracellular space of living brain tissue
751 is based on FLIM of a new Cl-sensitive fluorophore, ABP-dextran (Normoyle *et al.*, 2024).
752 These results are in contrast to the higher values measured using ion sensitive electrodes
753 (Jiang *et al.*, 1992; Kroeger *et al.*, 2010), a discrepancy that we cannot definitively explain at this
754 time. The ABP-dextran fluorophore is based on a validated structure (Biwersi *et al.*, 1992) and
755 was calibrated against Cl, other anions, and direct chemical analysis of chloride concentrations
756 in situ (Figures 1&2). ABP-dextran FLIM accurately reported Cl values in sulfated carbohydrate
757 polymers (Figure 2), so it is unlikely that the gangliosides, sGAGs or other anions in the
758 extracellular environment (Figure 1C) affected the accuracy of the ABP-dextran FLIM. ABP-
759 dextran overcomes several barriers to accurate measurement of extracellular chloride, including
760 sufficient sensitivity in the relevant range of chloride concentrations, competition with
761 autofluorescence, and exclusion from the cytoplasmic space, where lower chloride values would
762 be encountered. ABP-dextran was clearly excluded from the intracellular space (Figure 3A&B;
763 Figure 4A&C; Figure 6D) and blood vessels (Figure 6C,D&E). Experiments were focused on
764 establishing the utility of ABP-dextran as an extracellular-specific sensor and did not include
765 transgenic fluorophores that could have measured Cl^-_i and marked neurons for *in vivo* analysis.
766 We speculate that the difference between our non-invasive, novel fluorophore-based measures
767 and the implanted ion-sensitive electrode measures of Cl^-_o may arise from the large difference in
768 sample sizes, where microelectrodes sample a single microenvironment while the fluorometric
769 technique samples millions. It is much easier to perceive the wide distribution of Cl^-_o with the
770 larger sample size (Figure 4D), and to appreciate the average Cl^-_o. A study directly comparing
771 fluorometric and microelectrode techniques would be of great interest.

772 Stable Donnan exclusion

773 An important finding in this study is that Cl microdomains established by Donnan exclusion are
774 stable for weeks, and do not require active transport to be maintained (Figure 2). This
775 phenomenon is well-established in biophysics (Epsztein *et al.*, 2018; Gao *et al.*, 2022), but is
776 more confusing in neuronal physiology where membranes with time-varying ionic permeabilities
777 and transporters create a more complex environment (Voipio *et al.*, 2014; Doyon *et al.*, 2016;
778 Düsterwald *et al.*, 2018; Rahmati *et al.*, 2021). A point of particular confusion is the role of
779 active Cl transport vs. Donnan exclusion in maintaining a particular E_{GABA} in the face of GABA-
780 gated Cl flux that alters the local Cl concentration. After a GABA-gated Cl influx, and re-
781 establishment of local charge balance by cationic flux via voltage- and ligand-gated cation
782 channels, the local cytoplasm will contain excess chloride salts. This Cl has two fates: either
783 excess salt diffuses through the cytoplasm to re-establish a new equilibrium with fixed charges,
784 or the excess salt is transported back across the membrane by cation-chloride cotransporters
785 (Brumback & Staley, 2008; Lewin *et al.*, 2012; Doyon *et al.*, 2016; Beckstein & Naughton, 2022).
786 The transporters are required to re-establish the original steady state volume, but in the
787 absence of transport, diffusion maintains local Cl concentrations remarkably well (Brumback &
788 Staley, 2008; Rahmati *et al.*, 2021). In the absence of membrane Cl salt transport, this diffusion
789 of excess Cl salts will be associated with either a cytoplasmic volume increase from associated
790 water influx or an increase in the mean Cl concentration in the cytoplasm. At pathologically high
791 rates of Cl influx, membrane chloride salt transport becomes rate-limiting (Staley & Proctor,
792 1999; Jedlicka *et al.*, 2011; Lewin *et al.*, 2012; Doyon *et al.*, 2016), and chloride concentrations
793 become sufficiently labile to depolarize E_{GABA} (Barker & Ransom, 1978; Alger & Nicoll, 1982;

Huguenard & Alger, 1986; Staley *et al.*, 1995). Thus Donnan exclusion *establishes* the local value of E_{GABA}, and active transport *maintains* that value (and neuronal volume) in the face of synaptic Cl flux (Glykys *et al.*, 2014a). The same principals should apply to the local extracellular chloride concentrations described here, with astrocytic chloride buffering (Egawa *et al.*, 2013) and diffusion between the extracellular fluid, the CSF, and vascular spaces (Rasmussen *et al.*, 2022) taking the place of neuronal membrane cation-chloride cotransport. Importantly, because E_{GABA} is set by the ratio of Cl^-_o to Cl^-_i (as given by the Nernst equation) and neurons can actively adjust intracellular immobile anions (Rahmati *et al.*, 2021), there is no Cl^-_o level that expressly precludes hyperpolarizing inhibition because proportional Cl^-_i reduction allows E_{GABA} to be maintained at any given value (Figure 7). Multi-ion modeling from our group has previously demonstrated similarly modest changes in E_{GABA} with Cl^-_o reduction that can be counteracted by even more modest Cl^-_i changes (Glykys *et al.*, 2017).

Low extracellular Cl

The Cl^-_o measured by ABP FLIM is less than half of the canonical Cl^-_o. Such a low value of Cl^-_o should affect not only E_{GABA} but also the inhibitory $GABA_A$ conductance, because there are only half as many ions to carry the outward membrane currents (i.e. inward Cl- flux) (Coombs *et al.*, 1955). Shouldn't such a low value of Cl^-_o have been obvious from electrophysiological studies? E_{GABA} is determined by the ratio of Cl^-_i to Cl^-_o (Coombs *et al.*, 1955; Staley, 2023). If either concentration is known, the other can be determined from E_{GABA}. However if both Cl^-_i and Cl^-_o are determined by the concentrations of local immobile anions, neither can be set experimentally and thus E_{GABA} cannot be used to determine either Cl^-_i or Cl^-_o; only the ratio can be inferred from the Nernst equation. Similarly, although the conductance of inward Cl flux (outward membrane current) is determined in part by Cl^-_o, it is also determined by the $GABA_A$ permeability, i.e. the number of open membrane channels and their capacity for ion flux. Thus membrane currents are not sufficient to determine Cl^-_o (Coombs *et al.*, 1955). Control of the ionic milieu is greater in single-channel recordings, but whether the complement of immobile anions is physiological under these conditions is difficult to determine, and even in these conditions there is substantial uncertainty regarding local ionic concentrations (Li *et al.*, 2015). The effects of variable Cl^-_i and Cl^-_o have on E_{GABA} have been explored (Glykys *et al.*, 2017), but high resolution spatiotemporal correlation of all three parameters will provide exciting new insights into dendritic signal processing.

Cl^-_o microdomains

The extracellular matrix of the brain is often depicted as perineural nets surrounding parvalbumin neurons that are detected by specific agglutinins and antibodies (Celio & Blümcke, 1994). However, these assays detect very specific motifs of glycoproteins and glycosaminoglycan sulfation; using more permissive ionic methods, a highly anionic extracellular matrix can be seen to surround virtually all neurons (Golgi, 1898; Glykys *et al.*, 2014a; Morawski *et al.*, 2015). This extracellular matrix fills the extracellular space, which comprises about 20% of the brain's volume (Syková & Nicholson, 2008; Tønnesen *et al.*, 2018). We have focused our analysis on the sGAG moiety of proteoglycans because these are prominent constituents of perineuronal extracellular matrix (Tønnesen *et al.*, 2018; Karamanos *et al.*, 2021), are found in both dense and more diffuse neuronal extracellular matrix (Deepa *et al.*, 2006), and are readily perturbed experimentally with commercially available enzymes. GAGs are polymers of widely varied length comprised of sugars and substituted sugars (N-acetylglucosamine, glucuronic acid, and galactose) that are synthesized without templates. Up

839 to 3 sulfates are added to the sugar moieties before export to the extracellular space. This
840 enables the creation of a stable but highly variable spatial distribution of dense, fixed anionic
841 charge in the extracellular matrix. Figure 3 demonstrates that this variance is substantial at the
842 level of resolution of light microscopy. We have previously demonstrated reduction of fixed
843 extracellular anions after chondroitinase treatment (Glykys et al., 2014a), and others have
844 demonstrated small but significant depolarizing shifts of E_{GABA} after chondroitinase treatment
845 (Klein et al., 2018). However, the distribution of fixed anions at the extracellular face of $GABA_A$
846 receptors, and the corresponding Cl^-_o, is currently unknown. The effects of variable Cl^-_o and Cl^-_i
847 have on E_{GABA} have been explored (Glykys *et al.*, 2017), but high resolution spatiotemporal
848 correlation of all three variables would allow more descriptive modeling in complex solutions.

849 Physiological implications

850 Along with Cl^-_i microdomains (Rahmati *et al.*, 2021), Cl^-_o microdomains in the region of the
851 extracellular openings of $GABA_A$ receptor-operated channels are a critical determinant of both
852 E_{GABA} and the $GABA_A$ conductance. The wide range of Cl^-_o values established via Donnan
853 exclusion by sulfated GAGs (Figures 2, 3, 4, 5 and 6) makes possible a substantial variety of
854 effects of $GABA_A$ receptor activation based on the direction of chloride flux. These effects range
855 from hyperpolarizing inhibition through shunting inhibition through excitation by activation of low
856 threshold calcium currents and removal of the magnesium block of the NMDA receptor. In
857 addition, the effects of Cl^-_o on the quantity of charge that is carried by $GABA_A$ membrane
858 currents (the conductance) (Coombs *et al.*, 1955) makes possible a broad range of strengths of
859 $GABA_A$ synapses that is independent of the number or subunit composition of receptors or their
860 posttranslational modifications.

861 The turnover of the macromolecules comprising the extracellular matrix is very slow (Tsien,
862 2013), on the order of months to years based on rodent experiments (Margolis & Margolis,
863 1973) as well as the rate of deterioration of patients with genetic defects of GAG catabolism
864 (Héron *et al.*, 2011; Hampe *et al.*, 2020; Seo *et al.*, 2020). This slow turnover provides a
865 mechanism for long-lasting influences on synaptic GABA signaling. Some elements of GAG
866 synthesis are activity dependent (Sidharthan *et al.*, 2013), but currently nothing is known about
867 the insertion of GAGs into the extracellular matrix, in situ modification, and the capacity for
868 directed alterations of Cl^-_o microdomains in the regions of $GABA_A$ receptors and synapses. Thus
869 the role of extracellular chloride microdomains in synaptic signal processing and memory
870 remains to be discovered.

871 Pathological implications

872 Cytotoxic cerebral edema: If Cl^-_o is normally only half of the value of Cl in CSF and plasma, then
873 the capacity for Cl^-_o to increase acutely may be an important and hitherto unappreciated
874 element of the pathophysiology of cerebral edema (Glykys *et al.*, 2017). Matrix
875 metalloproteinases (MMPs) are released and activated after neuronal injury and death (Zhang
876 *et al.*, 2016). Release of sulfates in sGAGs from the extracellular matrix would reduce the
877 Donnan exclusion of Cl by fixed sulfates. This would result in an acute increase of Cl^-_o as in
878 Figure 4. The action of equilibrative cation-Cl cotransporters would then lead to a
879 corresponding increase in chloride salts in the cytoplasm of neighboring healthy neurons, with
880 attendant volume increases. This novel mechanism of cytotoxic edema could potentially be
881 ameliorated by pharmacological MMP inhibition. Alternatively, inhibition of the influx of chloride

882 salts that cross the BBB from the vascular space (Jha *et al.*, 2019) would limit the influx of Cl
883 into the extra and intracellular spaces.

884 Post Traumatic Epilepsy: Richard Miles and colleagues demonstrated that $GABA_A$ receptor
885 activation could be excitatory in human brain tissue resected for control of medically intractable
886 epilepsy (Cohen *et al.*, 2002). However, the pathomechanism has never been elucidated
887 (Huberfeld *et al.*, 2007; González, 2016; Karlócai *et al.*, 2016). Gliosis is the most common
888 finding in medically intractable epilepsy (Thom, 2014). In glial scars, reactive astrocytes
889 synthesize new matrix elements (Roll & Faissner, 2014; Song & Dityatev, 2018). If the
890 replacement matrix was more heavily sulfated than the original, as would be expected from the
891 firm texture that is responsible for the name "scar" (Lesperance *et al.*, 1992), then in areas of
892 gliosis Cl^-_o would be low. Low Cl^-_o could contribute to degradation of $GABA_A$ receptor mediated
893 inhibition, frank excitation, and failure of anticonvulsants whose action are predicated on intact
894 synaptic inhibition. Thus replacement of the extracellular matrix and distortion of extracellular
895 chloride microdomains could comprise an important mechanism of medically intractable
896 epilepsy after brain injury.

897 <u>Future studies</u>

898 The findings that Cl^-_o is both lower than expected and spatially heterogenous opens the door for
899 many investigations into the mechanisms by which Cl^-_o is set, such as the synthesis, export, and
900 in situ modification of sulfated GAGs. The activity dependence of these mechanisms and the
901 effect of Cl^-_o microdomains on synaptic signaling are additional areas of investigation.
902 Pathologically, the impact of changes in Cl^-_o in both acute edema and long-term complications
903 such as epilepsy may provide much-needed therapeutic insights into these frequently-
904 intractable conditions.

905

<u>Figure 1</u> Characterization and Calibration of Chloride-Sensitive Fluorophore ABP. ***A)*** N-(**a**mmonium)-**b**utyl **p**henanthridine (ABP) is synthesized in-house and conjugated to activated 10KDa dextran, a glucose polymer, at a molar ratio of 4.4. ***B)*** Representative calibration of ABP-dextran fluorescence lifetime versus Cl^- demonstrating ABP-dextran sensitivity to chloride-induced quenching. Calibration of ABP-dextran fluorescence lifetime vs Cl^-_o is displayed as a violin plot with mean +/- standard deviation overlaid. ABP-dextran lifetime at 0mM chloride (τ_o) is extrapolated using a best-fit approach (see Methods). ***C)*** Stern-Volmer plot demonstrates a linear relationship between ABP-dextran fluorescence lifetime and concentration of chloride and was used to convert lifetimes to chloride concentrations. The ratio of unquenched ABP-dextran fluorescence lifetime (τ_o) to ABP-dextran lifetime at a given concentration of quencher (τ) is plotted versus concentration of quencher (τ_o/τ vs $[Q^-]$). The slope of the linear regression is the Stern-Volmer constant (k_{SV}) which allows conversion of ABP-dextran lifetime to concentration of quencher, specifically Cl^- (blue circles / black line; k_{SV}=15.9M^{-1}). Four biologically relevant anions were found to have no experimentally relevant effect on ABP-dextran fluorescence lifetime: bicarbonate (k_{SV}=1.21M^{-1}), gluconate (k_{SV}=0.70M^{-1}), methyl sulfonate (k_{SV}=0.18M^{-1}), and phosphate (k_{SV}=0.11M^{-1}). Gluconate was subsequently used as a chloride substitute in non-standard aCSF formulations used for calibrations.

<u>Figure 2</u> Effects of immobile sulfate on Cl^- in a volume of agarose gel. ***A)*** Experimental schematic demonstrating how polysaccharide gels, cast in aCSF separately, were equilibrated in aCSF after transfer to a common vessel. Gels were either equilibrated with aCSF containing ABP-dextran, processed for chemical analysis, or subjected to multiple investigations in tandem (see Methods). ***B)*** We covalently bound sulfate groups to algal biopolymer agarose and cast this as a gel in aCSF to model perineuronal interstitial matrix that is rich in chondroitin sulfate-decorated glycosaminoglycans. We compared sulfated agarose gel to native agar and agarose gels, achieving a 250-fold increase in sulfate content compared to commercially available agar (bar 3 vs bar 1, respectively; $p < 0.001$, Student's paired *t*-test of at least three gel pieces' mean of technical replicates; note discontinuous y-axis). Commercially available agarose, which is intended as a sulfate-free product, had no measurable sulfate content (bar 2) and subsequently was used as a control gel. ***C)*** Chloride concentration was reduced in sulfated agarose gels. Cl^- was measured using both a standard colorimetric assay (dark gray bars) and ABP-dextran FLIM (light gray bars) in aCSF control (leftmost pair), within non-sulfated agarose gel (center pair) and within sulfated agarose gel containing ≈50mM (49.2+/-0.289mM) covalently bound sulfate (rightmost pair). Measured chemically or using ABP-dextran FLIM, Cl^- in sulfated agarose gels differed significantly from aCSF ($p = 0.00264$ and $p < 0.001$, respectively) and non-sulfated agarose gels ($p = 0.00354$ and $p < 0.001$, respectively), while Cl^- measured in non-sulfated agarose gels was not significantly different from aCSF when measured by chemical assay ($p = 0.190$) but registered a small but significant difference (3.5% increased Cl- relative to aCSF, $p = 0.00328$) when measured with ABP-dextran FLIM. Chemical assay and aCSF FLIM data points are averages of three technical replicants, while gel values are averaged measurements from each quadrant of a given gel, each compared using Student's paired *t*-test. ***D)*** Significant chloride concentration differences between agarose gels with 50mM covalently bound sulfate (dark blue) and non-sulfated agarose gels (light blue) do not equilibrate with time but instead are stable for as long as experimentally observed (> 3 weeks). ANOVA testing with Bonferroni correction demonstrates that Cl^- significantly differs between native agarose and sulfated agarose at all time points (overall and each pair $p < 0.001$) while neither agarose (each $p = 1.0000$) nor sulfated agarose gels (from left to right, $p = 1.0000$; $p = 0.2119$; $p = 0.1129$) change significantly with time. Cl- measurements from each quadrant of a given gel are averaged to generate each data point. ***E)*** Demonstration of stable juxtaposition of significantly different chloride concentrations at equilibrium. Separately cast sulfated and non-sulfated gel pieces are placed in a single vessel as described in ***A*** and equilibrated in common aCSF with ABP-dextran. Sulfated agarose gels (dark blue) again contain significantly lower Cl^- than do non-sulfated agarose gels (light blue; $p < 0.001$) or perfusate aCSF (gray; $p < 0.001$) in this representative experiment, while Cl^- within non-sulfated agarose gels is again not significantly different than perfusate aCSF ($p = 0.0647$). , Fields from each quadrant of each gel co-incubated in a single vessel with shared aCSF are analyzed using Student's paired *t*-test. *Statistical significance indicated on graph for p-values <0.05 (*); <0.01 (**); <0.001 (***); "ns" indicates "not significant". Error bars reflect standard deviation from the mean. Use of parametric tests confirmed appropriate via Jarque-Bera test (see Methods).*

966

967 **<u>Figure 3</u> Cl^- in the extracellular space is not uniform and is considerably lower than aCSF**
968 **perfusate.** ***A)*** High-magnification OHSC intensity image of ABP-dextran excluded from cell
969 bodies in the pyramidal cell layer (CA1; scale bar 20μm). ***B)*** Chloride-composite image again
970 demonstrating the exclusion of ABP-dextran from intracellular spaces as well as the non-
971 uniformity of Cl^-_o in the pyramidal cell layer of a representative OHSC. Representative pyramidal
972 cell visible just above and left of image center, identified by ABP-dextran exclusion and
973 morphology of resulting silhouette, is one of 6-10 neurons per field deemed to have a regular
974 and nearly-continuous border analyzed as described in ***D&E*** (scale bar 20μm). ***C)*** Histogram of
975 full field Cl^-_o in OHSC pictured in ***B***, demonstrating non-uniformity visually apparent in ***B***.
976 Notably, Cl^-_o = 44.5+/-15.9mM despite perfusate $[Cl^-]$ = 136mM (across all depths of this slice Cl^-
977 $_o$ = 49.7+/-18.5mM; mean +/- SD). ***D)*** Change in chloride ($\Delta[Cl^-]_o$) plotted against distance in the
978 perineuronal space (blue line) or the same trace overlaid onto a calibration aCSF FLIM image
979 (red line) corresponding to the perineuronal trace in ***B***. $\Delta[Cl^-]_o$ of calibration aCSF (red)
980 encapsulates machine and experimental noise, and $\Delta[Cl^-]_o$ in the perineuronal space (blue)
981 exceeds that of control in this representative neuron. ***E)*** Perineuronal $\Delta[Cl^-]_o$ per micron
982 calculated from many neurons' circumferential traces demonstrates that the variability of
983 perineuronal Cl^-_o in living *in vitro* system exceeds the variability of control aCSF (72 neurons
984 versus matched calibration aCSF controls from depths of 20-100μm in this representative
985 OHSC; $p < 0.001$, by Kolmogorov-Smirnov test). *Cl^-_o image rendering and presentation details*
986 *can be found in Methods and in subsequent figures. Scale bars A&B: 20μm.*

987

988 **<u>Figure 4</u> Generation of composite chloride images and cell body masking for pixel**
989 **quantification.** ***A)*** ABP-dextran intensity data of an OHSC, derived by taking the total number
990 of photons detected in each pixel throughout the acquisition period, is used to inform on tissue
991 structure. Image series ***A-C*** corresponds to Figure 3B and its traced neuron example. Neuron
992 silhouette traced in ***B&C*** is indicated with a white asterisk. ***B)*** Cl^-_o calculated from ABP-dextran
993 lifetime. The loss of discernible structure is due to the fact that the intensity of the ABP-dextran
994 signal has no effect on the Cl^-_o calculated from fluorescence lifetime (see Methods). Areas
995 corresponding to cell body silhouettes in ***A*** have notable pixelation with relatively high apparent
996 Cl^-_o values interspersed with black pixels, the latter indicating statistical exclusion due to low
997 signal intensity (see Methods). ***C)*** In order to observe Cl^-_o with spatial context restored, we use
998 intensity data to inform the brightness of the raw chloride data in ***B***, generating a composite
999 image in which the color corresponds to Cl^-_o and brightness is attenuated based on the intensity
1000 of the signal in each pixel (see Methods). The most popular proprietary FLIM software packages
1001 use similar methods of composite data display. Note that prior to Cl^-_o analysis a further intensity-
1002 based thresholding step excludes pixels from inside somatic silhouettes in the focal plane, and
1003 pixels not corresponding to the slice (i.e., perfusate, top left) are also excluded by manually
1004 drawn ROI (masks not shown). ***D)*** Histogram of Cl^-_o in all analyzed pixels (blue) versus pixels
1005 excluded through thresholding step, principally marking somatic silhouettes (gray) in this
1006 representative OHSC, demonstrating no secondary peak at typical Cl^-_i values (i.e., =< 15mM).
1007 Further, this range of low Cl^-_o values is more likely excluded (gray) than included (blue) in our
1008 analysis (indicated by gray arrow). ***E&F)*** To further verify the cellular exclusion of ABP-dextran,
1009 we looked specifically at the margins of well-defined somatic silhouettes, such as the example
1010 marked across ***A-C***, to search for signs of intracellular ABP-dextran leakage. We compared
1011 perineuronal pixels up to 1mm outside neurons to those pixels which lie inside the somatic
1012 margins of 72 neurons but were not excluded prior to thresholding (statistically excluded pixels
1013 are not considered; see Methods). Consistent with out-of-focus extracellular ABP-dextran, we
1014 found similar calculated Cl^-_o values between the two groups (***E***) with the expected wider
1015 variance in the less intense intracellular signal (***F***; see text). *Scale bar:* ***A-C*** *50μm.*

1016

1017 **<u>Figure 5</u> Chondroitinase treatment removes fixed perineuronal anions and attenuates Cl^-_o**
1018 **displacement.** Cl^-_o composite images of representative mouse hippocampus slice cultures
1019 imaged in culture media (Cl^- ≈ 64mM) with 1mg/mL ABP-dextran (100mM ABP-Dextran) before
1020 (***A***) and after (***B***) treatment with bacterial MMP analog chondroitinase, or after sham digestion
1021 (***C***); shared colorbar for ***A-C*** at right. ***D)*** Histograms of $[Cl^-]_o$ corresponding to ***A&B*** demonstrate
1022 pre-chondroitinase digestion (dark blue) and post-chondroitinase digestion (light blue) $[Cl^-]_o$
1023 populations of pixels are significantly different ($p < 0.001$ by Kolmogorov-Smirnov paired-sample
1024 test). ***E)*** When images from ***A&B*** are broken into regularly shaped regions of interest and
1025 analyzed as paired groups, pre-chondroitinase and post-chondroitinase are again significantly
1026 different (46.7+/-2.7mM vs 55.0+/- 5.0mM, respectively, mean+/-SD; $p = 0.0152$ by Wilcoxon
1027 rank sum test). ***F)*** Violin plot of data from ***A&B*** (dark and light blue, respectively) vs grouped
1028 sham-digested slice data (gray) demonstrating that Cl^-_o increases significantly after chondroitin
1029 sulfate is removed by digestion, whether compared to pre-digestion of the same slice or a sham
1030 digestion (each $p < 0.001$ by Kolmogorov-Smirnov paired-sample test). ***G)*** Measurement of
1031 glycosaminoglycans, including chondroitin sulfate, released into the perfusate after OHSCs are
1032 treated with chondroitinase (vs sham digestion) using a commercial colorimetric assay. A
1033 significantly higher concentration of polyanionic glycosaminoglycans are found in the
1034 extracellular fluid after chondroitinase digestion ($p = 0.00632$ by Student's paired *t*-test),
1035 consistent with the release of chondroitin sulfate from extracellular matrix within slice cultures
1036 and a resultant increase in Cl^-_o. ***H)*** HPLC analysis confirms the presence of chondroitin sulfate
1037 released into digestion buffer after chondroitinase treatment (mean = 0.20μg/mL); there was no
1038 detectable chondroitin sulfate in sham digests, negating formal significance testing. ***A-C*** *scale*
1039 *bars 50μm; all slice cultures were DIV14-21 at time of experiment; cultures were grown directly*
1040 *on glass with the exception of* ***G*** *where cultures were grown on membrane inserts (see*
1041 *Methods); significance values noted graphically for p-values <0.05 (*); <0.01 (**); <0.001 (***);*
1042 *"ns" indicates "not significant". Note that data contained in* ***D-F*** *labeled 'pre' and 'post' are*
1043 *derived from OHSCs in* ***A*** *and* ***B****, respectively.*

1044

1045

1046 **<u>Figure 6</u> *In vivo* Cl^-_o in mouse neocortex is consistent with *ex vivo* findings. *A&B)***
1047 Schematic of *in vivo* imaging set-up, using a surgically implanted headbar to immobilize P26-
1048 P30 mouse pup for imaging through 3mm coverglass window overlaying 1% agar brought up in
1049 aCSF containing ABP-Dextran and 136mM chloride laid directly on exposed cortex. ***C)*** Intensity
1050 image of mouse L1 cortex (depth 54μm) demonstrating ABP-dextran diffusion into parenchyma
1051 and exclusion from vessels. ***D)*** Intensity image of L2/3 cortex 138μm deep to ***C***, demonstrating
1052 ABP-dextran exclusion from cells and vessels; large vessels appear blurred because their
1053 widest diameter exists superficial to this field (depth 192μm). Inset is 7x zoomed portion of
1054 corresponding chloride composite image, one of three fields from this animal from which we
1055 identified and analyzed pyramidal neurons in a manner similar to Figure 3. ***E)*** Region of interest
1056 (ROI) selections shown numbered in Cl^-_o composite image, corresponding to intensity image in
1057 ***C***, demonstrates exclusion of large vessels from ROIs but is otherwise permissive. ***F)*** Change in
1058 chloride ($\Delta[Cl^-]_o$) plotted against distance in the perineuronal space (blue line) or the same trace
1059 overlaid onto a calibration aCSF FLIM image (red line) of the representative neuron traced in ***D***
1060 inset (white dashes). ***G)*** Perineuronal $\Delta[Cl^-]_o$ per micron calculated from 11 L2/3 neurons'
1061 circumferential traces demonstrates that the variability of perineuronal Cl^-_o *in vivo* exceeds the
1062 variability of control aCSF ($p < 0.001$, by Kolmogorov-Smirnov test; 11 neurons from 3 fields of
1063 1 animal; see *Methods*), consistent with our *in vitro* findings. ***H)*** Cl^-_o in mouse neocortex is
1064 significantly lower than the CSF Cl^- as shown in this violin plot of all ROI pixels with population
1065 mean (black dashed lines) and overlaid mean+/-standard error of ROIs analyzed. Compared to
1066 agarose brought up in 136mM aCSF overlying the cortex (leftmost violin plot: 135.4+/-5.0mM;
1067 mean+/-standard deviation of all analyzed pixels), *in vivo* mouse cortex had significantly lower
1068 Cl^-_o whether measured in cellular fields such as in ***C*** or in acellular fields such as in ***D*** (plots 2
1069 and 3: 48.9+/-6.7mM and 55.0+/-17.9mM, respectively). This was true when considering all
1070 ROIs in all fields from the animal from which ***C&D*** were taken (plot 4: 47.2+/-14.9mM), and
1071 when considering all fields from all animals used in this study (plot 5: 48.1+/-17.0mM).
1072 Statistically comparing discreet ROI means by ANOVA analysis with Bonferroni correction (red
1073 overlay indicating mean+/-standard error of ROIs), all groups demonstrated a statistically
1074 significant difference vs control ($p < 0.001$) but were not significantly different vs each other ($p =$
1075 1.0000). Note that ROIs are too numerous to display for all groups, and we have instead
1076 overlaid the mean+/-standard error (red lines) associated with ANOVA analysis of ROIs. Violin
1077 plot means (dashed black lines), reflecting aggregated pixels from all ROIs, appear on the
1078 graph; associated standard deviations are listed above but are not explicitly labeled on graph.
1079 *Scale bars **C,D&E**: 50μm; inset scale bar D: 5μm; significance values noted graphically for p-*
1080 *values <0.05 (*); <0.01 (**); <0.001 (***); "ns" indicates "not significant".*

1081

<u>Figure 7</u> E_{GABA} is maintained at any Cl^-_o given proportionate change in Cl^-_i. The reversal potential of chloride across $GABA_A$Rs (E_{GABA}) is given by the Nernst equation, $E = \frac{RT}{zF} \ln\left(\frac{Clo}{Cli}\right)$. At constant temperature the only variables that determine E_{GABA} are Cl^-_o and Cl^-_i, or rather the only single variable is the ratio of Cl^-_o to Cl^-_i. Using the Nernst equation to model E_{GABA} across the physiological range of Cl^-_i at several Cl^-_o values, we unsurprisingly find that hyperpolarizing E_{GABA} values can be achieved at any Cl^-_o value. Lower Cl^-_o values simply need a proportionately lower Cl^-_i value to achieve a given E_{GABA}, which neurons are capable of by increasing intracellular immobile anions such as cytoskeletal biopolymers (Rahmati *et al.*, 2021). In the examples given above, the Cl^-_i necessary to maintain E_{GABA} of -85mV (dashed red line) varies from 1mM to 6mM as Cl^-_o is varied from 20mM to 120mM. More complex multi-ion modeling will be facilitated with higher resolution and spatiotemporally correlated measurements of Cl^-_o and Cl^-_i in proximity across the neuronal membrane.

1096 Bibliography

1097 Alger BE & Nicoll RA. (1982). Pharmacological evidence for two kinds of GABA receptor on rat
1098 hippocampal pyramidal cells studied in vitro. *J Physiol* **328,** 125-141.

1099
1100 Barker JL & Ransom BR. (1978). Amino acid pharmacology of mammalian central neurones grown in
1101 tissue culture. *J Physiol* **280,** 331-354.

1102
1103 Beckstein O & Naughton F. (2022). General principles of secondary active transporter function. *Biophys*
1104 *Rev (Melville)* **3,** 011307.

1105
1106 Berdichevsky Y, Saponjian Y, Park KI, Roach B, Pouliot W, Lu K, Swiercz W, Dudek FE & Staley KJ. (2016).
1107 Staged anticonvulsant screening for chronic epilepsy. *Ann Clin Transl Neurol* **3,** 908-923.

1108
1109 Biwersi J, Farah N, Wang YX, Ketcham R & Verkman AS. (1992). Synthesis of cell-impermeable Cl-
1110 sensitive fluorescent indicators with improved sensitivity and optical properties. *Am J Physiol*
1111 **262,** C242-250.

1112
1113 Biwersi J, Tulk B & Verkman AS. (1994). Long-wavelength chloride-sensitive fluorescent indicators. *Anal*
1114 *Biochem* **219,** 139-143.

1115
1116 Brumback AC & Staley KJ. (2008). Thermodynamic regulation of NKCC1-mediated Cl- cotransport
1117 underlies plasticity of GABA(A) signaling in neonatal neurons. *J Neurosci* **28,** 1301-1312.

1118
1119 Celio MR & Blümcke I. (1994). Perineuronal nets--a specialized form of extracellular matrix in the adult
1120 nervous system. *Brain Res Brain Res Rev* **19,** 128-145.

1121
1122 Celio MR, Spreafico R, De Biasi S & Vitellaro-Zuccarello L. (1998). Perineuronal nets: past and present.
1123 *Trends Neurosci* **21,** 510-515.

1124
1125 Chahine NO, Chen FH, Hung CT & Ateshian GA. (2005). Direct measurement of osmotic pressure of
1126 glycosaminoglycan solutions by membrane osmometry at room temperature. *Biophys J* **89,**
1127 1543-1550.

1128
1129 Che A & De Marco García NV. (2021). An in vivo Calcium Imaging Approach for the Identification of Cell-
1130 Type Specific Patterns in the Developing Cortex. *Front Neural Circuits* **15,** 747724.

1131
1132 Cohen I, Navarro V, Clemenceau S, Baulac M & Miles R. (2002). On the origin of interictal activity in
1133 human temporal lobe epilepsy in vitro. *Science* **298,** 1418-1421.

1134

1135 Coombs JS, Eccles JC & Fatt P. (1955). The specific ionic conductances and the ionic movements across
1136 the motoneuronal membrane that produce the inhibitory post-synaptic potential. *J Physiol* **130,**
1137 326-374.

1138

1139 Deepa SS, Carulli D, Galtrey C, Rhodes K, Fukuda J, Mikami T, Sugahara K & Fawcett JW. (2006).
1140 Composition of perineuronal net extracellular matrix in rat brain: a different disaccharide
1141 composition for the net-associated proteoglycans. *J Biol Chem* **281,** 17789-17800.

1142

1143 DiRaddo JO, Miller EJ, Bowman-Dalley C, Wroblewska B, Javidnia M, Grajkowska E, Wolfe BB, Liotta DC &
1144 Wroblewski JT. (2015). Chloride is an Agonist of Group II and III Metabotropic Glutamate
1145 Receptors. *Mol Pharmacol* **88,** 450-459.

1146

1147 Doyon N, Vinay L, Prescott SA & De Koninck Y. (2016). Chloride regulation: a dynamic equilibrium crucial
1148 for synaptic inhibition. *Neuron* **89,** 1157-1172.

1149

1150 Düsterwald KM, Currin CB, Burman RJ, Akerman CJ, Kay AR & Raimondo JV. (2018). Biophysical models
1151 reveal the relative importance of transporter proteins and impermeant anions in chloride
1152 homeostasis. *Elife* **7**.

1153

1154 Ebihara S, Shirato K, Harata N & Akaike N. (1995). Gramicidin-perforated patch recording: GABA
1155 response in mammalian neurones with intact intracellular chloride. *J Physiol* **484 (Pt 1),** 77-86.

1156

1157 Egawa K, Yamada J, Furukawa T, Yanagawa Y & Fukuda A. (2013). Cl^- homeodynamics in gap junction-
1158 coupled astrocytic networks on activation of GABAergic synapses. *J Physiol* **591,** 3901-3917.

1159

1160 Epsztein R, Shaulsky E, Dizge N, Warsinger DM & Elimelech M. (2018). Role of Ionic Charge Density in
1161 Donnan Exclusion of Monovalent Anions by Nanofiltration. *Environ Sci Technol* **52,** 4108-4116.

1162

1163 Fatin-Rouge N, Milon A, Buffle J, Goulet RR & Tessier A. (2003). Diffusion and partitioning of solutes in
1164 agarose hydrogels: the relative influence of electrostatic and specific interactions. *The Journal of*
1165 *Physical Chemistry B* **107,** 12126-12137.

1166

1167 Florence TM & Farrar YJ. (1971). Spectrophotometric determination of chloride at the parts-per-billion
1168 level by the mercury(II) thiocyanate method. *Analytica chimica acta* **54,** 373--377.

1169

1170 Frantz C, Stewart KM & Weaver VM. (2010). The extracellular matrix at a glance. *J Cell Sci* **123,** 4195-
1171 4200.

1172

1173 Fuse T & Toshiya S. (1975). Preparation and properties of agar sulfates. *Agricultural and biological*
1174 *chemistry* **39,** 119--126.

1175

Gao KW, Yu X, Darling RM, Newman J & Balsara NP. (2022). Increased Donnan exclusion in charged polymer networks at high salt concentrations. *Soft Matter* **18,** 282-292.

Gehlen MH. (2020). The centenary of the Stern-Volmer equation of fluorescence quenching: From the single line plot to the SV quenching map. *Journal of photochemistry and photobiology C, Photochemistry reviews* **42,** 100338.

Glykys J, Dzhala V, Egawa K, Balena T, Saponjian Y, Kuchibhotla K, Bacskai B, Kahle K, Zeuthen T & Staley K. (2014a). Local impermeant anions establish the neuronal chloride concentration. *Science* **343,** 670-675.

Glykys J, Dzhala V, Egawa K, Balena T, Saponjian Y, Kuchibhotla KV, Bacskai BJ, Kahle KT, Zeuthen T & Staley KJ. (2014b). Response to comments on "Local impermeant anions establish the neuronal chloride concentration". *Science* **345,** 1130.

Glykys J, Dzhala V, Egawa K, Kahle KT, Delpire E & Staley K. (2017). Chloride dysregulation, seizures, and cerebral edema: a relationship with therapeutic potential. *Trends in neurosciences* **40,** 276-294.

Golgi C. (1898). Intomo alla struttura delle cellule nervose. *Boll Soc Med-Chir Pavia* **1,** 1-14.

González MI. (2016). Regulation of the cell surface expression of chloride transporters during epileptogenesis. *Neurosci Lett* **628,** 213-218.

Gregor HP. (1951). Gibbs-Donnan equilibria in ion exchange resin systems. *Journal of the American Chemical Society* **73,** 642-650.

Grimley JS, Li L, Wang W, Wen L, Beese LS, Hellinga HW & Augustine GJ. (2013). Visualization of synaptic inhibition with an optogenetic sensor developed by cell-free protein engineering automation. *J Neurosci* **33,** 16297-16309.

Hampe CS, Eisengart JB, Lund TC, Orchard PJ, Swietlicka M, Wesley J & McIvor RS. (2020). Mucopolysaccharidosis Type I: A Review of the Natural History and Molecular Pathology. *Cells* **9**.

Helfferich F. (1995). *Ion Exchange*. Dover, New York, NY.

Hrabetová S, Masri D, Tao L, Xiao F & Nicholson C. (2009). Calcium diffusion enhanced after cleavage of negatively charged components of brain extracellular matrix by chondroitinase ABC. *J Physiol* **587,** 4029-4049.

Hu H, Gan J & Jonas P. (2014). Interneurons. Fast-spiking, parvalbumin^{+} GABAergic interneurons: from cellular design to microcircuit function. *Science* **345,** 1255263.

1217
1218 Huberfeld G, Wittner L, Clemenceau S, Baulac M, Kaila K, Miles R & Rivera C. (2007). Perturbed chloride
1219 homeostasis and GABAergic signaling in human temporal lobe epilepsy. *J Neurosci* **27,** 9866-
1220 9873.

1221
1222 Huguenard JR & Alger BE. (1986). Whole-cell voltage-clamp study of the fading of GABA-activated
1223 currents in acutely dissociated hippocampal neurons. *J Neurophysiol* **56,** 1-18.

1224
1225 Héron B, Mikaeloff Y, Froissart R, Caridade G, Maire I, Caillaud C, Levade T, Chabrol B, Feillet F, Ogier H,
1226 Valayannopoulos V, Michelakakis H, Zafeiriou D, Lavery L, Wraith E, Danos O, Heard JM &
1227 Tardieu M. (2011). Incidence and natural history of mucopolysaccharidosis type III in France and
1228 comparison with United Kingdom and Greece. *Am J Med Genet A* **155a,** 58-68.

1229
1230 Jedlicka P, Deller T, Gutkin BS & Backus KH. (2011). Activity-dependent intracellular chloride
1231 accumulation and diffusion controls GABA(A) receptor-mediated synaptic transmission.
1232 *Hippocampus* **21,** 885-898.

1233
1234 Jha RM, Kochanek PM & Simard JM. (2019). Pathophysiology and treatment of cerebral edema in
1235 traumatic brain injury. *Neuropharmacology* **145,** 230-246.

1236
1237 Jiang C, Agulian S & Haddad GG. (1992). Cl- and Na+ homeostasis during anoxia in rat hypoglossal
1238 neurons: intracellular and extracellular in vitro studies. *J Physiol* **448,** 697-708.

1239
1240 Kaneko H, Putzier I, Frings S, Kaupp UB & Gensch T. (2004). Chloride accumulation in mammalian
1241 olfactory sensory neurons. *J Neurosci* **24,** 7931-7938.

1242
1243 Karamanos NK, Theocharis AD, Piperigkou Z, Manou D, Passi A, Skandalis SS, Vynios DH, Orian-Rousseau
1244 V, Ricard-Blum S, Schmelzer CEH, Duca L, Durbeej M, Afratis NA, Troeberg L, Franchi M, Masola
1245 V & Onisto M. (2021). A guide to the composition and functions of the extracellular matrix. *Febs*
1246 *j* **288,** 6850-6912.

1247
1248 Karlócai MR, Wittner L, Tóth K, Maglóczky Z, Katarova Z, Rásonyi G, Erőss L, Czirják S, Halász P, Szabó G,
1249 Payne JA, Kaila K & Freund TF. (2016). Enhanced expression of potassium-chloride cotransporter
1250 KCC2 in human temporal lobe epilepsy. *Brain Struct Funct* **221,** 3601-3615.

1251
1252 Klein PM, Lu AC, Harper ME, McKown HM, Morgan JD & Beenhakker MP. (2018). Tenuous Inhibitory
1253 GABAergic Signaling in the Reticular Thalamus. *J Neurosci* **38,** 1232-1248.

1254
1255 Kroeger D, Tamburri A, Amzica F & Sík A. (2010). Activity-dependent layer-specific changes in the
1256 extracellular chloride concentration and chloride driving force in the rat hippocampus. *J*
1257 *Neurophysiol* **103,** 1905-1914.

1258
1259 Kuang D & Hampson DR. (2006). Ion dependence of ligand binding to metabotropic glutamate receptors.
1260 *Biochem Biophys Res Commun* **345,** 1-6.

1261
1262 Kuner T & Augustine GJ. (2000). A genetically encoded ratiometric indicator for chloride: capturing
1263 chloride transients in cultured hippocampal neurons. *Neuron* **27,** 447-459.

1264
1265 Kusama N, Harding AM & Benson CJ. (2010). Extracellular chloride modulates the desensitization
1266 kinetics of acid-sensing ion channel 1a (ASIC1a). *J Biol Chem* **285,** 17425-17431.

1267
1268 Lawrence R, Olson SK, Steele RE, Wang L, Warrior R, Cummings RD & Esko JD. (2008). Evolutionary
1269 differences in glycosaminoglycan fine structure detected by quantitative glycan reductive
1270 isotope labeling. *J Biol Chem* **283,** 33674-33684.

1271
1272 Lesperance LM, Gray ML & Burstein D. (1992). Determination of fixed charge density in cartilage using
1273 nuclear magnetic resonance. *J Orthop Res* **10,** 1-13.

1274
1275 Lewin N, Aksay E & Clancy CE. (2012). Computational modeling reveals dendritic origins of GABA(A)-
1276 mediated excitation in CA1 pyramidal neurons. *PLoS One* **7,** e47250.

1277
1278 Li M, Toombes GE, Silberberg SD & Swartz KJ. (2015). Physical basis of apparent pore dilation of ATP-
1279 activated P2X receptor channels. *Nat Neurosci* **18,** 1577-1583.

1280
1281 Lin R, Kwok JC, Crespo D & Fawcett JW. (2008). Chondroitinase ABC has a long-lasting effect on
1282 chondroitin sulphate glycosaminoglycan content in the injured rat brain. *J Neurochem* **104,** 400-
1283 408.

1284
1285 Margolis RK & Margolis RU. (1973). The turnover of hexosamine and sialic acid in glycoproteins and
1286 mucopolysaccharides of brain. *Biochim Biophys Acta* **304,** 413-420.

1287
1288 Marinsky JA. (1985). An interpretation of the sensitivity of weakly acidic (basic) polyelectrolyte (cross-
1289 linked and linear) equilibria to excess neutral salt. *Journal of physical chemistry (1952)* **89,** 5294--
1290 5302.

1291
1292 Morawski M, Reinert T, Meyer-Klaucke W, Wagner FE, Tröger W, Reinert A, Jäger C, Brückner G &
1293 Arendt T. (2015). Ion exchanger in the brain: quantitative analysis of perineuronally fixed anionic
1294 binding sites suggests diffusion barriers with ion sorting properties. *Scientific reports* **5,** 16471.

1295
1296 Nicholson C & Kraig RP. (1975). Chloride and potassium changes measured during spreading depression
1297 in catfish cerebellum. *Brain Res* **96,** 384-389.

1298

1299 Normoyle KP, Lillis KP & Staley KJ. (2024). Synthesis and Characterization of a Novel Concentration-
1300 Independent Fluorescent Chloride Indicator, ABP-Dextran, Optimized for Extracellular Chloride
1301 Measurement. *Biomolecules* **14**.

1302
1303 Orlando C, Ster J, Gerber U, Fawcett JW & Raineteau O. (2012). Perisynaptic chondroitin sulfate
1304 proteoglycans restrict structural plasticity in an integrin-dependent manner. *J Neurosci* **32,**
1305 18009-18017, 18017a.

1306
1307 Plested AJ & Mayer ML. (2007). Structure and mechanism of kainate receptor modulation by anions.
1308 *Neuron* **53,** 829-841.

1309
1310 Rahmati N, Normoyle KP, Glykys J, Dzhala VI, Lillis KP, Kahle KT, Raiyyani R, Jacob T & Staley KJ. (2021).
1311 Unique Actions of GABA Arising from Cytoplasmic Chloride Microdomains. *J Neurosci* **41,** 4957-
1312 4975.

1313
1314 Rasmussen MK, Mestre H & Nedergaard M. (2022). Fluid transport in the brain. *Physiol Rev* **102,** 1025-
1315 1151.

1316
1317 Reuter D, Zierold K, Schröder WH & Frings S. (1998). A depolarizing chloride current contributes to
1318 chemoelectrical transduction in olfactory sensory neurons in situ. *J Neurosci* **18,** 6623-6630.

1319
1320 Roll L & Faissner A. (2014). Influence of the extracellular matrix on endogenous and transplanted stem
1321 cells after brain damage. *Front Cell Neurosci* **8,** 219.

1322
1323 Sato SS, Artoni P, Landi S, Cozzolino O, Parra R, Pracucci E, Trovato F, Szczurkowska J, Luin S & Arosio D.
1324 (2017). Simultaneous two-photon imaging of intracellular chloride concentration and pH in
1325 mouse pyramidal neurons in vivo. *Proceedings of the National Academy of Sciences* **114,** E8770-
1326 E8779.

1327
1328 Schnaar RL, Gerardy-Schahn R & Hildebrandt H. (2014). Sialic acids in the brain: gangliosides and
1329 polysialic acid in nervous system development, stability, disease, and regeneration. *Physiol Rev*
1330 **94,** 461-518.

1331
1332 Seo JH, Okuyama T, Shapiro E, Fukuhara Y & Kosuga M. (2020). Natural history of cognitive development
1333 in neuronopathic mucopolysaccharidosis type II (Hunter syndrome): Contribution of genotype to
1334 cognitive developmental course. *Mol Genet Metab Rep* **24,** 100630.

1335
1336 Sidharthan NP, Minchin RF & Butcher NJ. (2013). Cytosolic sulfotransferase 1A3 is induced by dopamine
1337 and protects neuronal cells from dopamine toxicity: role of D1 receptor-N-methyl-D-aspartate
1338 receptor coupling. *J Biol Chem* **288,** 34364-34374.

1339

1340 Sola M, Kneussel M, Heck IS, Betz H & Weissenhorn W. (2001). X-ray crystal structure of the trimeric N-
1341 terminal domain of gephyrin. *J Biol Chem* **276,** 25294-25301.

1342
1343 Song I & Dityatev A. (2018). Crosstalk between glia, extracellular matrix and neurons. *Brain Res Bull* **136,**
1344 101-108.

1345
1346 Staley K. (2023). Ionic mechanisms of ictogenic disinhibition. In *Jasper's Basic Mechanisms of the*
1347 *Epilepsies*. In Press.

1348
1349 Staley KJ & Mody I. (1992). Shunting of excitatory input to dentate gyrus granule cells by a depolarizing
1350 GABAA receptor-mediated postsynaptic conductance. *J Neurophysiol* **68,** 197-212.

1351
1352 Staley KJ & Proctor WR. (1999). Modulation of mammalian dendritic GABA(A) receptor function by the
1353 kinetics of Cl- and HCO3- transport. *J Physiol* **519 Pt 3,** 693-712.

1354
1355 Staley KJ, Soldo BL & Proctor WR. (1995). Ionic mechanisms of neuronal excitation by inhibitory GABAA
1356 receptors. *Science* **269,** 977-981.

1357
1358 Stoppini L, Buchs PA & Muller D. (1991). A simple method for organotypic cultures of nervous tissue. *J*
1359 *Neurosci Methods* **37,** 173-182.

1360
1361 Svennerholm L. (1980). Gangliosides and synaptic transmission. *Adv Exp Med Biol* **125,** 533-544.

1362
1363 Syková E & Nicholson C. (2008). Diffusion in brain extracellular space. *Physiol Rev* **88,** 1277-1340.

1364
1365 Thom M. (2014). Review: Hippocampal sclerosis in epilepsy: a neuropathology review. *Neuropathol Appl*
1366 *Neurobiol* **40,** 520-543.

1367
1368 Thompson SM, Deisz RA & Prince DA. (1988). Relative contributions of passive equilibrium and active
1369 transport to the distribution of chloride in mammalian cortical neurons. *J Neurophysiol* **60,** 105-
1370 124.

1371
1372 Titze J, Shakibaei M, Schafflhuber M, Schulze-Tanzil G, Porst M, Schwind KH, Dietsch P & Hilgers KF.
1373 (2004). Glycosaminoglycan polymerization may enable osmotically inactive Na+ storage in the
1374 skin. *Am J Physiol Heart Circ Physiol* **287,** H203-208.

1375
1376 Tora AS, Rovira X, Cao AM, Cabayé A, Olofsson L, Malhaire F, Scholler P, Baik H, Van Eeckhaut A,
1377 Smolders I, Rondard P, Margeat E, Acher F, Pin JP & Goudet C. (2018). Chloride ions stabilize the
1378 glutamate-induced active state of the metabotropic glutamate receptor 3. *Neuropharmacology*
1379 **140,** 275-286.

Torres PB, Nagai A, Jara CEP, Santos JP, Chow F & dos Santos DYAC. (2021). Determination of sulfate in algal polysaccharide samples: a step-by-step protocol using microplate reader. *Ocean and Coastal Research* **69**.

Tremblay R, Lee S & Rudy B. (2016). GABAergic Interneurons in the Neocortex: From Cellular Properties to Circuits. *Neuron* **91,** 260-292.

Tsien RY. (2013). Very long-term memories may be stored in the pattern of holes in the perineuronal net. *Proc Natl Acad Sci U S A* **110,** 12456-12461.

Tyzio R, Minlebaev M, Rheims S, Ivanov A, Jorquera I, Holmes GL, Zilberter Y, Ben-Ari Y & Khazipov R. (2008). Postnatal changes in somatic γ-aminobutyric acid signalling in the rat hippocampus. *European Journal of Neuroscience* **27,** 2515-2528.

Tønnesen J, Inavalli V & Nägerl UV. (2018). Super-Resolution Imaging of the Extracellular Space in Living Brain Tissue. *Cell* **172,** 1108-1121.e1115.

Urban JP, Maroudas A, Bayliss MT & Dillon J. (1979). Swelling pressures of proteoglycans at the concentrations found in cartilaginous tissues. *Biorheology* **16,** 447-464.

Verkman AS. (1990). Development and biological applications of chloride-sensitive fluorescent indicators. *Am J Physiol* **259,** C375-388.

Voipio J, Boron WF, Jones SW, Hopfer U, Payne JA & Kaila K. (2014). Comment on "Local impermeant anions establish the neuronal chloride concentration". *Science* **345,** 1130.

Xiao F, Nicholson C, Hrabe J & Hrabetová S. (2008). Diffusion of flexible random-coil dextran polymers measured in anisotropic brain extracellular space by integrative optical imaging. *Biophys J* **95,** 1382-1392.

Zhang S, Kojic L, Tsang M, Grewal P, Liu J, Namjoshi D, Wellington CL, Tetzlaff W, Cynader MS & Jia W. (2016). Distinct roles for metalloproteinases during traumatic brain injury. *Neurochem Int* **96,** 46-55.

Zhang YW, Uchendu S, Leone V, Bradshaw RT, Sangwa N, Forrest LR & Rudnick G. (2021). Chloride-dependent conformational changes in the GlyT1 glycine transporter. *Proc Natl Acad Sci U S A* **118**.

1420

Additional Information:

Competing Interests: None of the authors have any competing interests to declare, as indicated during the submission process for each author individually.

Funding: This work was funded by three grants to Kevin J. Staley from the National Institute for Neurological Disorders and Stroke (NINDS): NIH R01 NS040109, R35 NS116852 and P01 NS127769.

Data availability statement: All data files used to generate the figures in the paper can be found on GitHub under KieranNormoyle/NeuronalChloride2023.

Author Contributions: KPN, KPL, KE and KJS conceived of and designed the approach and execution of these experiments. KPN and KJS are responsible for specific experimental design, interpretation of experiments, and manuscript preparation. KPL designed and built the two-photon microscopes and operational software that made this work possible. MAM and LL lent expertise and support for in vivo experiments, including training KPN in mouse cranial window surgery. LL and FHS provided expertise and critical input during experimental interpretation and manuscript writing. MP and BPC designed and executed HPLC experiments specific to this manuscript. This research was made possible by NINDS funding to KJS (NIH R01 NS040109, R35 NS116852 and P01 NS127769).

Authors' Translational Perspective: We hypothesized that if measured non-invasively, the extracellular chloride concentration (Cl^-_o) would be less than CSF chloride values (≈110mM) due to Donnan exclusion by heterogeneously distributed extracellular anions so that Cl^-_o would be lower than expected and heterogenous. We found that Cl^-_o has a mean value much lower than previously appreciated (≈50mM) and is indeed heterogenous. Our data further demonstrates that the loss of heterogenous sulfated glycosaminoglycans (sGAGs) in extracellular matrix results in an increased Cl^-_o as the Donnan equilibrium rebalances. Together with our previous work demonstrating heterogenous intracellular chloride (Cl^-_i), our data suggests the variance of GABA reversal potential (E_{GABA}) we and others have observed is due to the heterogeneity of the concentrations of the primary permeant anion, Cl^-, on both the intra- and extracellular side of the channel. Stable variations of perisynaptic Cl^-_o or Cl^-_i potentially allows for the tuning of E_{GABA} at individual $GABA_A$ synapses and suggests a mechanism for information storage. Pathophysiological alteration of Cl^-_o would be expected to occur when sGAG-containing extracellular matrix is damaged, such as when matrix metalloproteases (MMPs) are released following neuronal injury or death. The expected increase in extracellular chloride salts, in turn leading to equilibrative intracellular increases, represents a new mechanism of cytotoxic edema.

Acknowledgements: This work was supported by NIH R01 NS040109, NIH R35 NS116852, and NIH P01 NS127769 to KJS. The authors would like to thank current and former members of the Pediatric Epilepsy Research Laboratory at MGH for critical input, discussions, and support during experimental development including Joseph Glykys, Negah Rahmati, Trevor Balena, Rehan Raiyyani, and Michelle Mail. The authors would also like to thank members of the MGH Institute for Neurodegenerative Disorders, particularly Steven S. Hou, for technical expertise and related advice.

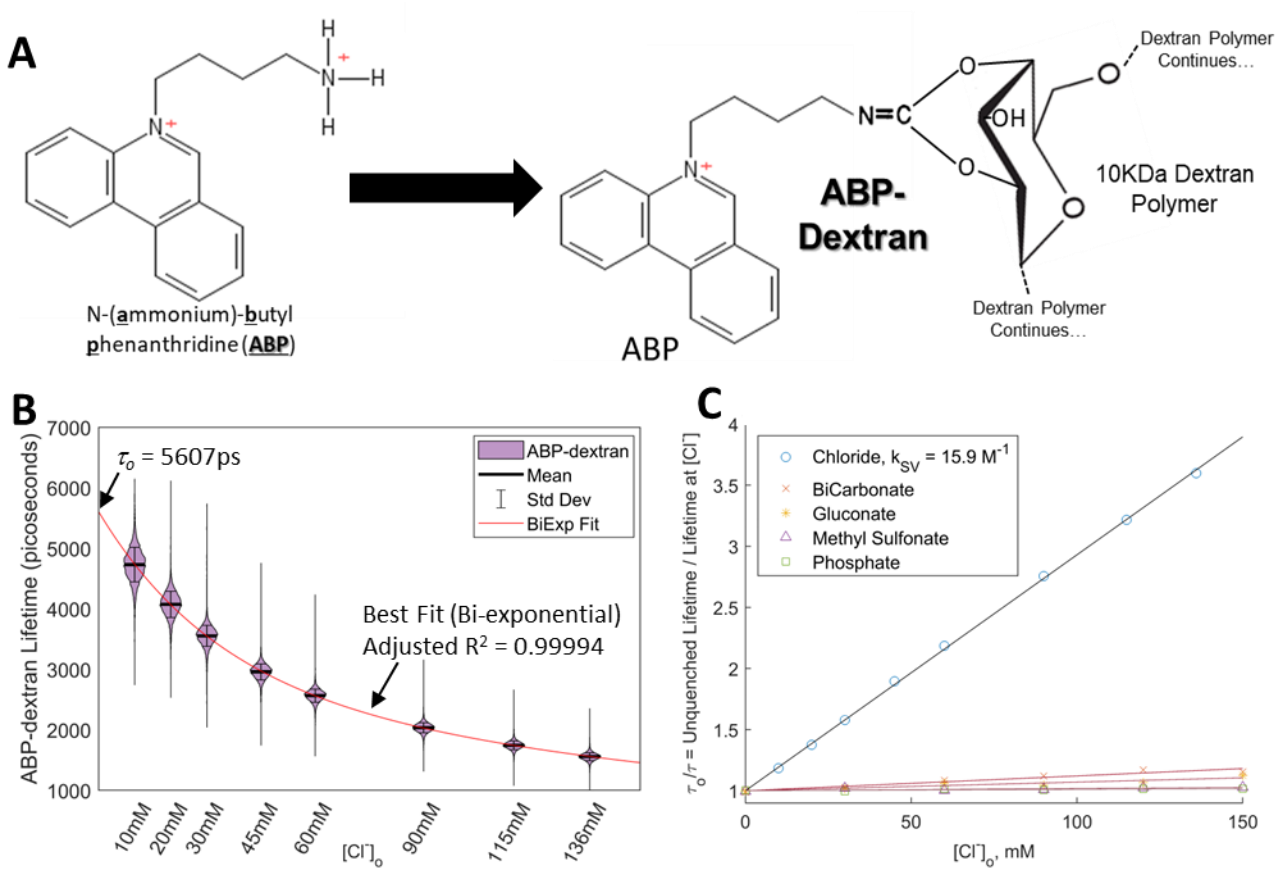
A
N-(ammonium)-butyl
phenanthridine (ABP)
ABP
ABP-
Dextran
Dextran Polymer
Continues…
10KDa Dextran
Polymer
Dextran Polymer
Continues…
B
ABP-dextran Lifetime (picoseconds)
τ_o = 5607ps
ABP-dextran
Mean
Std Dev
BiExp Fit
Best Fit (Bi-exponential)
Adjusted R^2 = 0.99994
10mM
20mM
30mM
45mM
60mM
$[Cl^-]_o$
90mM
115mM
136mM
C
τ_o/τ = Unquenched Lifetime / Lifetime at $[Cl^-]$
Chloride, k_{SV} = 15.9 M^{-1}
BiCarbonate
Gluconate
Methyl Sulfonate
Phosphate
$[Cl^-]_o$, mM

Figure 1

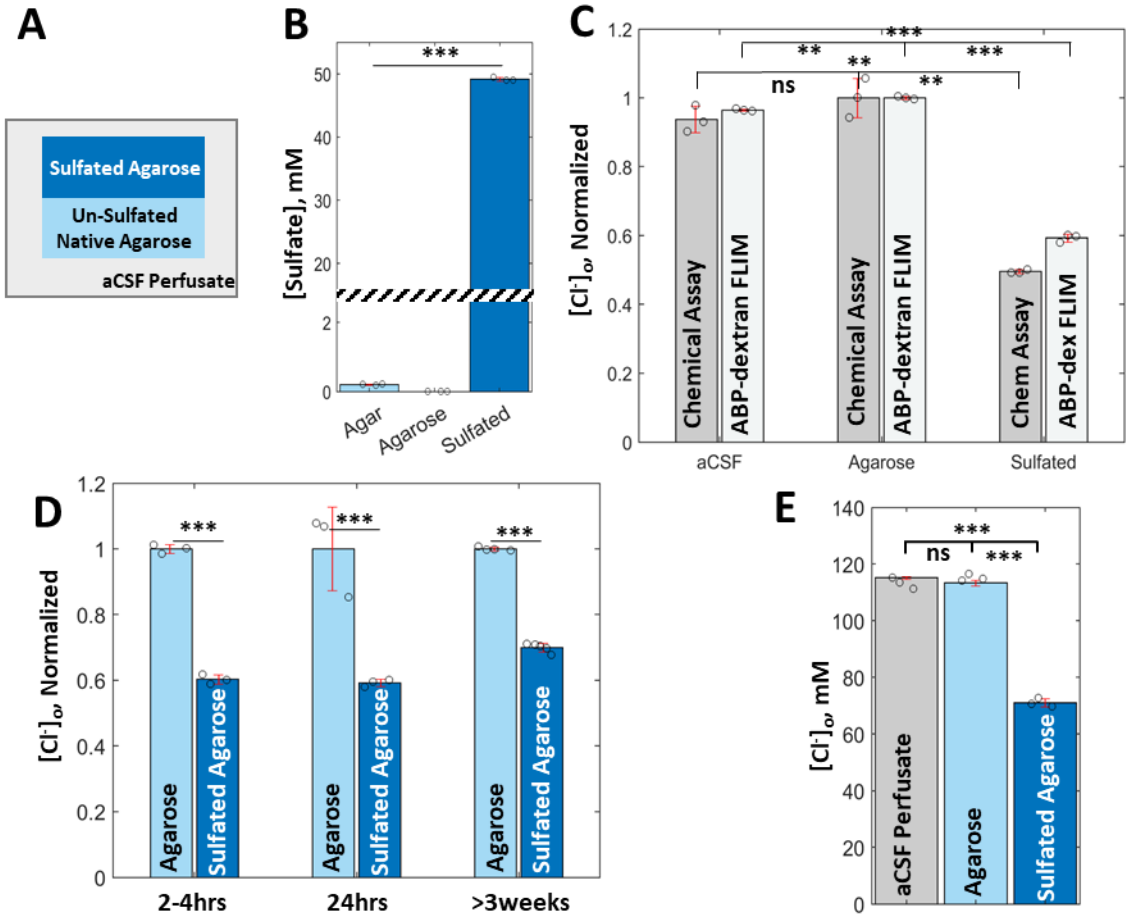
A
Sulfated Agarose
Un-Sulfated Native Agarose
aCSF Perfusate
B
[Sulfate], mM
Agar
Agarose
Sulfated
C
[Cl-]o, Normalized
Chemical Assay
ABP-dextran FLIM
Chemical Assay
ABP-dextran FLIM
Chem Assay
ABP-dex FLIM
aCSF
Agarose
Sulfated
ns
D
[Cl-]o, Normalized
Agarose
Sulfated Agarose
2-4hrs
24hrs
>3weeks
E
[Cl-]o, mM
aCSF Perfusate
Agarose
Sulfated Agarose
ns

Figure 2

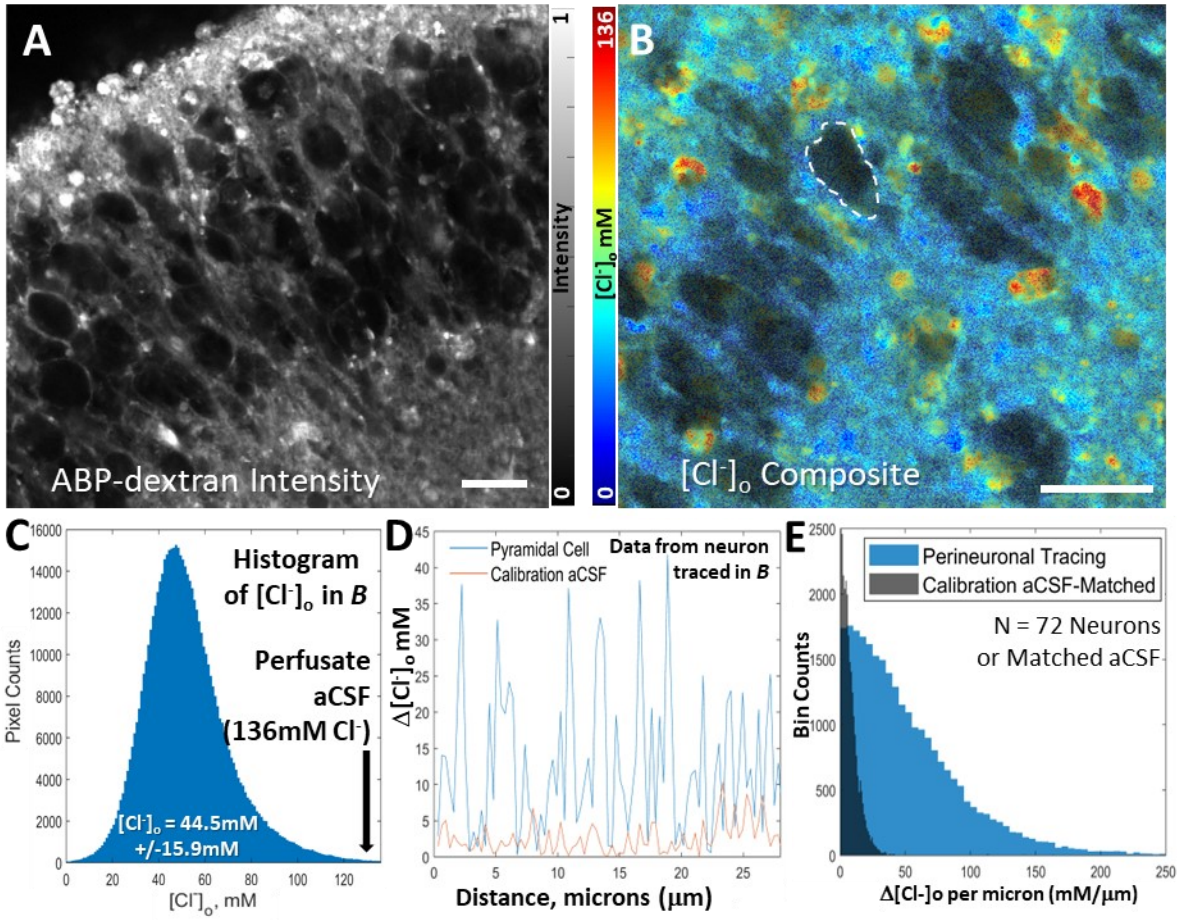
A
ABP-dextran Intensity
Intensity
1
0
B
[Cl-]o Composite
[Cl-]o mM
136
0
C
Histogram of [Cl-]o in B
Perfusate aCSF (136mM Cl-)
[Cl-]o = 44.5mM +/-15.9mM
Pixel Counts
[Cl-]o, mM
D
Pyramidal Cell
Calibration aCSF
Data from neuron traced in B
Δ[Cl-]o mM
Distance, microns (μm)
E
Perineuronal Tracing
Calibration aCSF-Matched
N = 72 Neurons or Matched aCSF
Bin Counts
Δ[Cl-]o per micron (mM/μm)

Figure 3

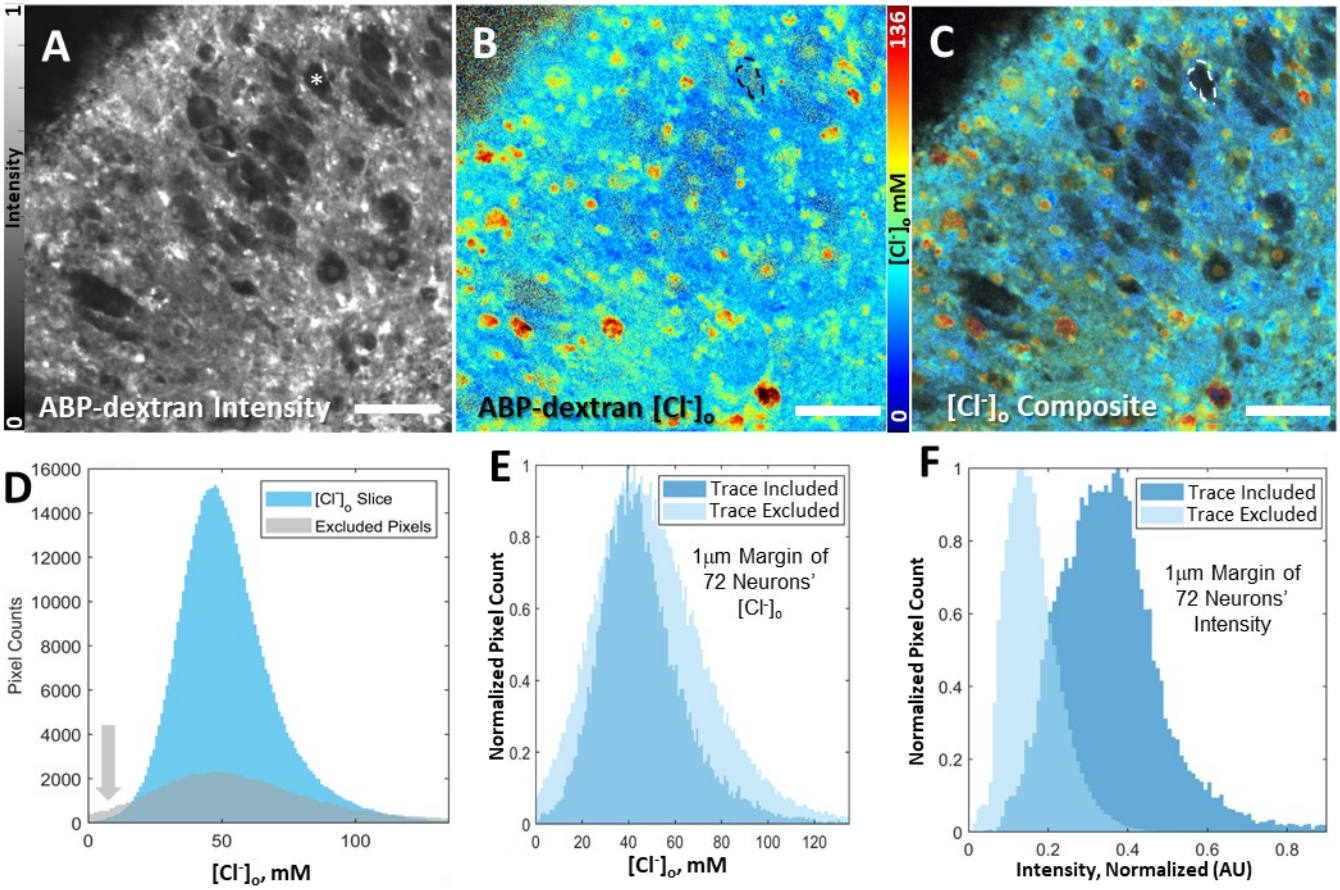
A
B
C
Intensity
1
0
ABP-dextran Intensity
ABP-dextran [Cl-]o
[Cl-]o mM
136
0
[Cl-]o Composite
D
[Cl-]o Slice
Excluded Pixels
Pixel Counts
[Cl-]o, mM
E
Trace Included
Trace Excluded
1μm Margin of 72 Neurons' [Cl-]o
Normalized Pixel Count
[Cl-]o, mM
F
Trace Included
Trace Excluded
1μm Margin of 72 Neurons' Intensity
Normalized Pixel Count
Intensity, Normalized (AU)

Figure 4

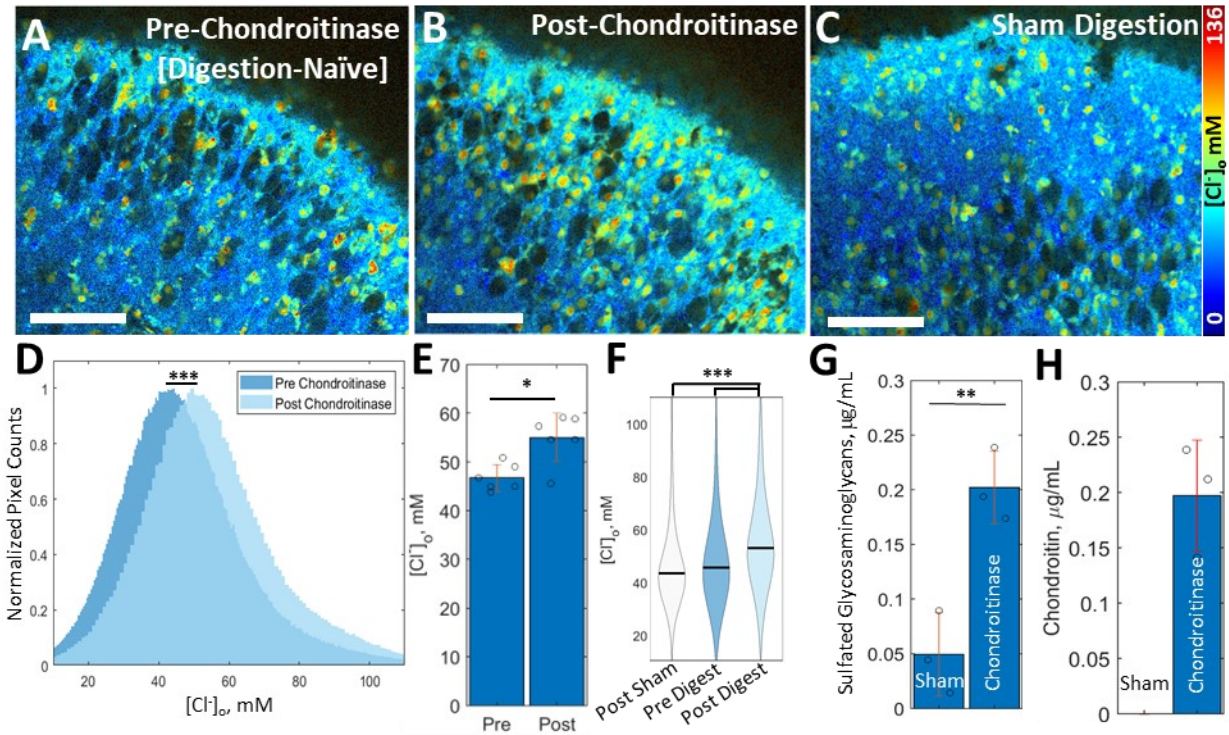
A
Pre-Chondroitinase
[Digestion-Naïve]
B
Post-Chondroitinase
C
Sham Digestion
136
[Cl-]o mM
0
D
***
Pre Chondroitinase
Post Chondroitinase
Normalized Pixel Counts
[Cl-]o, mM
E
*
[Cl-]o, mM
Pre
Post
F
***
[Cl-]o, mM
Post Sham
Pre Digest
Post Digest
G
**
Sulfated Glycosaminoglycans, µg/mL
Sham
Chondroitinase
H
Chondroitin, µg/mL
Sham
Chondroitinase

Figure 5

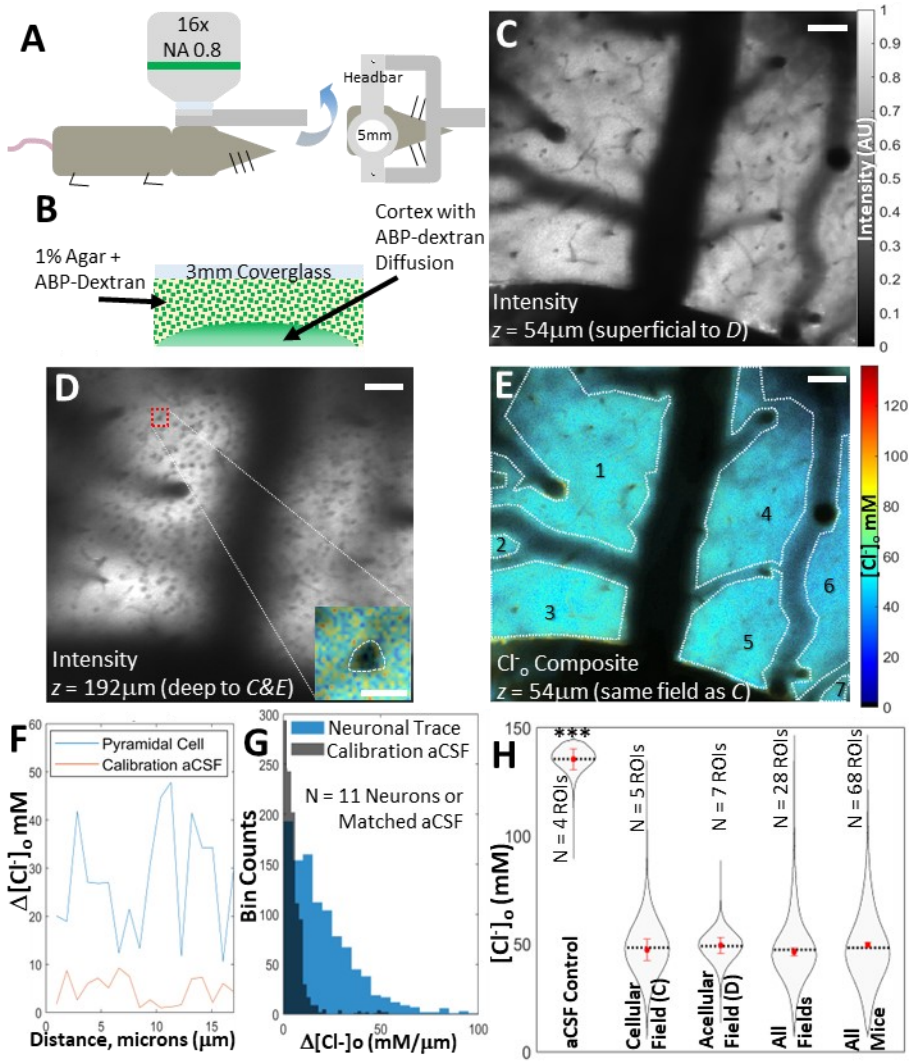
A
16x
NA 0.8
Headbar
5mm
B
1% Agar +
ABP-Dextran
3mm Coverglass
Cortex with
ABP-dextran
Diffusion
C
Intensity
z = 54µm (superficial to D)
Intensity (AU)
D
Intensity
z = 192µm (deep to C&E)
E
Cl-o Composite
z = 54µm (same field as C)
[Cl-]o mM
F
Pyramidal Cell
Calibration aCSF
Δ[Cl-]o mM
Distance, microns (µm)
G
Neuronal Trace
Calibration aCSF
N = 11 Neurons or
Matched aCSF
Bin Counts
Δ[Cl-]o (mM/µm)
H
***
N = 4 ROIs
N = 5 ROIs
N = 7 ROIs
N = 28 ROIs
N = 68 ROIs
[Cl-]o (mM)
aCSF Control
Cellular Field (C)
Acellular Field (D)
All Fields
All Mice

Figure 6

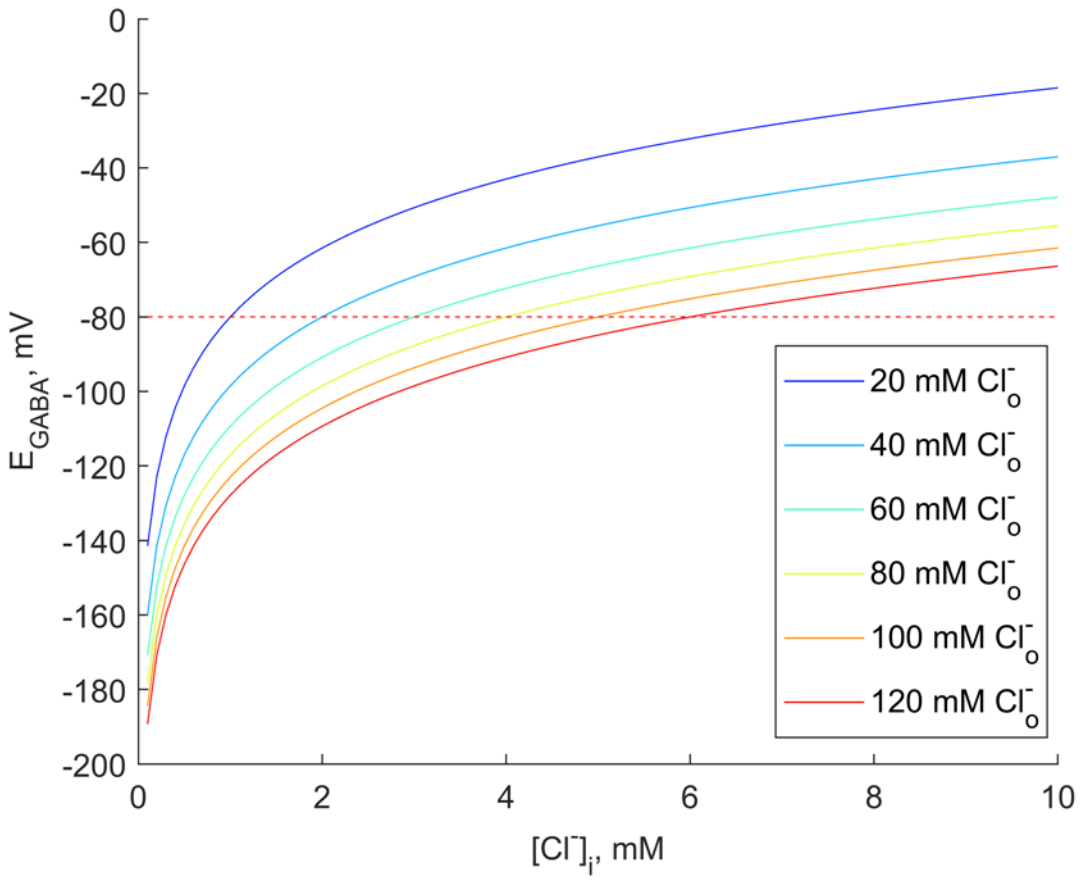
0
-20
-40
-60
-80
-100
-120
-140
-160
-180
-200
E_{GABA}, mV
0
2
4
6
8
10
$[Cl^-]_i$, mM
20 mM Cl^-_o
40 mM Cl^-_o
60 mM Cl^-_o
80 mM Cl^-_o
100 mM Cl^-_o
120 mM Cl^-_o

Figure 7